

Tunable critical correlations in kagome ice

A. A. Turrini ^{1,2}, A. Harman-Clarke,^{3,4} G. Haeseler,⁴ T. Fennell ^{1,*}, I. G. Wood ⁵, P. Henelius,^{6,7}
S. T. Bramwell,³ and P. C. W. Holdsworth⁴

¹Laboratory for Neutron Scattering and Imaging, Paul Scherrer Institut, 5232 Villigen PSI, Switzerland

²Department of Quantum Matter Physics, 24 Quai Ernest-Ansermet, 1211 Genève 4, Switzerland

³London Centre for Nanotechnology and Department of Physics and Astronomy, University College London, 17-19 Gordon Street, London WC1H 0AH, United Kingdom

⁴Université de Lyon, ENS de Lyon, CNRS, Laboratoire de Physique, 69342 Lyon, France

⁵Department of Earth Sciences, University College London, WC1E 6BT London, United Kingdom

⁶Department of Physics, Royal Institute of Technology, 106 91 Stockholm, Sweden

⁷Faculty of Science and Engineering, Åbo Akademi University, 20500 Åbo, Finland



(Received 9 February 2021; revised 27 January 2022; accepted 27 January 2022; published 2 March 2022)

We present a comprehensive experimental and theoretical study of the kagome ice Coulomb phase that explores the fine-tuning of critical correlations by applied field, temperature, and crystal orientation. The continuous modification of algebraic correlations is observed by polarized neutron scattering experiments and is found to be well described by numerical simulations of an idealized model. We further clarify the thermodynamics of field-tuned Kasteleyn transitions and demonstrate some dramatic finite-size-scaling properties that depend on how topological string defects wind around the system boundaries. We conclude that kagome ice is a remarkable example of a critical and topological state in a real system that may be subject to fine experimental control.

DOI: [10.1103/PhysRevB.105.094403](https://doi.org/10.1103/PhysRevB.105.094403)

I. INTRODUCTION

A. Context

Kagome ice [1,2] is a quasi-two-dimensional magnetic state with finite configurational entropy and algebraic correlations, which is formed when a magnetic field is applied along the cubic [111] direction of a spin ice such as $\text{Ho}_2\text{Ti}_2\text{O}_7$ and $\text{Dy}_2\text{Ti}_2\text{O}_7$. Theory [3] predicts kagome ice to be a topologically constrained Coulomb phase that, through small tilts of the applied field, can be tuned toward lines of unconventional Kasteleyn transitions, with associated anisotropic algebraic scaling. The physics of kagome ice is extremely rich and subtle, exemplifying departures from the usual Landau-Ginzburg-Wilson paradigm of continuous phase transitions in magnetism, towards alternative paradigms of topological constraint [4], hitherto only observed in soft matter [5]. Phase transitions and scaling in such topologically constrained systems are of great interest as they present new challenges to theory [6–8]. Yet experimental model systems are quite scarce and, in this sense, kagome ice, being a very clean and well-defined magnetic state that is easily controlled by applied field, is a most valuable example.

Over the years there have been extensive experimental investigations of the thermodynamic properties of kagome ice [2,9–12] as well as some neutron scattering studies of correlations [13–15]. Despite this, and detailed analytical studies [3], the understanding of kagome ice has significant gaps. In

this paper, we aim to complete the characterization of static correlations in kagome ice by means of a direct confrontation between theory, experiment, and numerical simulation. In particular, we present polarized neutron scattering experiments in the static approximation that we compare with our own thermodynamics and model simulations, as well as with the existing analytical predictions of Moessner and Sondhi [3]. In this way, we are able to elucidate some different properties of kagome ice and to subject the many theoretical predictions of Ref. [3] to a detailed test against simulation and experiment. We broadly confirm the theoretical picture, adding further structure to the predictions of Ref. [3].

B. Description of kagome ice

In a spin ice, Ising-like magnetic moments point in the local easy axis directions (the body diagonals of the tetrahedra of the pyrochlore lattice or $\langle 111 \rangle$ directions of the cubic unit cell) and their interaction energy is minimized by ensuring that the magnetic moments obey an ice rule, i.e., two spins point in and two point out of each tetrahedron (the two-in–two-out rule). This condition is equivalent to the ice rule that governs proton disorder in water ice [16,17]. The spins map onto the elements of a lattice field that captures this and whose configurations may be represented in terms of correlated loops that cannot be removed by stretching or bending. These topological constraints lead to a three-dimensional Coulomb phase [18–20], a classical spin liquid with emergent $U(1)$ symmetry, and associated dipolar correlations.

Referring to Fig. 1, when a magnetic field of moderate strength is applied in the [111] direction, it pins one quarter of

*Previously at Institut Laue Langevin, CS 20156, Cedex 9, 38042 Grenoble, France; tom.fennell@psi.ch

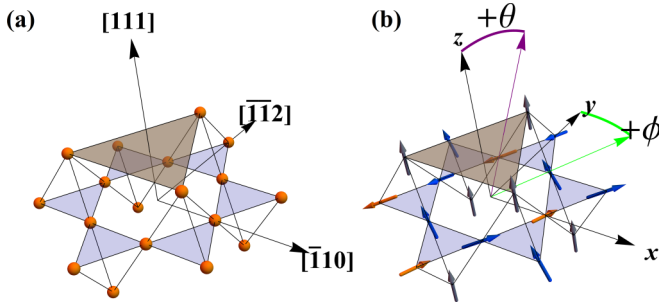


FIG. 1. (a) Section of the pyrochlore lattice showing the alternating kagome (blue) and triangular (gray) lattices and associated crystallographic axes. (b) Example of an ice-rule satisfying configuration of spins shows the field-pinned spins on the triangular layers (gray) and spins on the kagome layer that are oriented favorably (blue) and unfavorably (orange) with respect to the applied field. The three-dimensional ice rule (two in and two out on each tetrahedron) and two-dimensional (two in and one out or vice versa on each triangle) local ordering rule are both obeyed. The angles $\theta > 0$ and $\phi > 0$ are shown in purple and green respectively.

the spins which occupy the vertices of triangular [111] planes. The remaining three quarters of the spins occupy the vertices of kagome lattices, which are stacked alternately with the triangular planes. Because these spins make a shallow angle with the field and have a lesser Zeeman energy than the pinned spin, the ice rule can compete with the field such that one spin per triangle of the kagome plane has a component opposing the field, as also illustrated in Fig. 1. A subset of ice-rule states with reduced entropy [11] is selected and a magnetization plateau develops at $\frac{2}{3}$ of the eventual magnetization, which signals the kagome ice state [1,2,9]. When the field is strong enough to overwhelm the ice rule, the remaining field-opposing spin is reversed, forming a unique ice-rule-breaking configuration with three in (out) and one out (in) on every tetrahedron.

The characteristic magnetization plateau [2,9,10], reduced residual entropy, and entropy release at plateau termination [12] were originally identified in $\text{Dy}_2\text{Ti}_2\text{O}_7$, and the magnetization plateau was also identified in $\text{Ho}_2\text{Ti}_2\text{O}_7$ [14,21]. An interesting aspect of kagome ice is the liquid-gas-like critical point [9] that separates plateau termination by a first-order phase transition at low temperature from a more gradual crossover at higher temperature. The existence of this was first rationalized by the monopole theory of excitations in spin ices [22], in which it can be identified as the critical end point of the monopole crystallization transition [23]. Differences in the exact ratio of competing exchange and dipolar interactions result in a critical field that is somewhat lower in $\text{Dy}_2\text{Ti}_2\text{O}_7$ ($H_c \approx 0.9$ T) than in $\text{Ho}_2\text{Ti}_2\text{O}_7$ ($H_c \approx 1.6$ T).

C. Coulomb phase and Kasteleyn transition

As in the case of spin ice in zero field, we can distinguish a nearest-neighbor model of kagome ice in which spins are coupled ferromagnetically and where ice-rule-breaking defects carry no magnetic charge, from one which includes dipole interactions, which leads to a magnetic charge on each

defect. We will refer to both classes of topological defects as magnetic monopoles. In fact, the physics discussed in the present paper is almost entirely that of the vacuum for such defects, which is the Coulomb phase. Hence we concentrate on the nearest-neighbor model with ice-rule-breaking defects suppressed. One key signature of the Coulomb phase is the appearance of pinch points in the diffuse neutron scattering pattern of kagome ice, as observed in $\text{Ho}_2\text{Ti}_2\text{O}_7$ [14] and $\text{Dy}_2\text{Ti}_2\text{O}_7$ [13,15]. These pinch points occur at the zone center for the kagome lattice rather than that of the pyrochlore lattice, where the pinch points for spin ice [20] in zero field occur. This difference indicates the change from a three- to a two-dimensional Coulomb phase.

The topological nature of Coulomb phases [24] leads to unconventional phase transitions [6,25,26]. A particular example is the Kasteleyn transition, originally predicted for dimers on the honeycomb lattice [24,27,28] (which form a Coulomb phase [24,28]) and observed experimentally, to a good approximation, in a lipid bilayer phase transition [5]. Later, this transition was predicted to occur in both two- [3,29] and three-dimensional [30–33] settings in spin ice.

A finite concentration of monopoles destroys the topological phase transition and the associated thermodynamic singularities [31,33,34], so the transition is formally unobservable if the energy scale for monopole creation is finite. However, if the monopole concentration is small enough, the asymptotic approach to the transition is observable, but unless the dynamics is nonlocal, such as in the worm Monte Carlo algorithm discussed below, a finite monopole concentration is necessary to maintain equilibrium [33]. In real systems a best compromise is required between a low monopole concentration and ergodic evolution.

The connection between kagome ice and the honeycomb lattice dimer model was originally made by Moessner and Sondhi [3], who presented an analytical calculation of the spin-spin correlation functions in kagome ice, as well as a theory of the Kasteleyn transition. A key prediction of the theory is that the Kasteleyn transition would be accompanied by unconventional scaling of the generalized susceptibility, manifesting as the movement of certain features in the diffuse neutron scattering structure factor. Although some features of this theory have been observed [14], the detailed predictions of anisotropic scaling of algebraic correlations were not tested in previous work.

The kagome ice phase also corresponds to the KII phase of dipolar kagome spin ice [35,36]. For a discussion of this relationship, we refer the reader to Appendix A.

D. Plan of the paper

The plan of the paper is as follows. In Sec. II we review the relevant parts of the theory of Ref. [3] and add to this our analysis of the thermodynamic and critical properties. In Sec. III we describe our numerical simulations of kagome ice and its Kasteleyn transitions and in Sec. IV we describe our neutron scattering experiments and their comparison with the numerical simulations and the theory. Our main findings are discussed in Sec. V and we draw conclusions in Sec. VI.

II. THEORY

A. Kasteleyn transition

1. Model

Convenient axes for describing kagome ice are defined within the pyrochlore structure (Fig. 1) by the direction of the applied field, where the vertical direction is $z \parallel [111]$, and the two perpendicular horizontal directions spanning the kagome plane are $x \parallel [\bar{1}10]$ and $y \parallel [\bar{1}\bar{1}2]$; unit vectors in these directions are denoted by \hat{x} , \hat{y} , and \hat{z} . The field may be tilted away from z towards y by the angle θ , and any rotation of the resulting in-plane field component from y toward x is quantified by the angle ϕ . In this work, all fields are applied along $[111]$, selecting the Z_2^+ topological sector (as opposed to $[\bar{1}\bar{1}\bar{1}]$ and Z_2^- , respectively). Our system is further defined such that up tetrahedra have the spin in the triangular lattice above the kagome plane relative to the applied magnetic field along z and down tetrahedra the opposite; a triangle in the kagome plane derives its up/down identity from its tetrahedron.

The Zeeman energy of a spin in the presence of magnetic field \vec{B} is $E^B = -\vec{\mu} \cdot \vec{B}$, where $\vec{\mu}$ is the single-ion magnetic moment. When the field is exactly aligned in the $[111]$ direction with $\vec{B} = B\hat{z}$, for the kagome plane spins $E^B = \mp \frac{1}{3}|\vec{\mu}|B$, in the ratio 2:1, so the kagome ice microstates have equal probability. Tilting the field away from z towards y by an angle $\theta > 0$ gives a contribution to the Zeeman energy from the in-plane spin components, which singles out one sublattice in the kagome plane (labeled with index $\kappa = 1$) as the preferred location for the field-opposing spin while keeping the other sublattices ($\kappa = 2, 3$) equivalent [3,14,29]. The tilt can be further generalized by rotating in the x - y plane by an angle ϕ , which further lowers the symmetry, distinguishing all three sublattices.

2. Spins and pseudospins

Given that classical spin ice is built from discrete spin degrees of freedom, it often proves convenient to reformulate the problem in the language of an Ising model, introducing pseudospin degrees of freedom $\sigma_i = \pm 1$. Taking an up tetrahedron as the crystallographic basis, the four spins align with respect to the local axes $\vec{d}_0 = \frac{1}{\sqrt{3}}[111]$ (i.e., $\vec{d}_0 \parallel z$), $\vec{d}_1 = \frac{1}{\sqrt{3}}[\bar{1}\bar{1}1]$, $\vec{d}_2 = \frac{1}{\sqrt{3}}[\bar{1}1\bar{1}]$, and $\vec{d}_3 = \frac{1}{\sqrt{3}}[1\bar{1}\bar{1}]$ so that $\vec{d}_\kappa \cdot \vec{d}_0 = -\frac{1}{3}$. In the convention that $\sigma_i = 1$ corresponds to a spin pointing out, the pseudospin is defined

$$\sigma_i = \frac{\vec{\mu}_i \cdot \vec{d}_i}{|\vec{\mu}|}. \quad (1)$$

In terms of these variables, spin ice maps to an Ising antiferromagnet with two in and two out becoming two down and two up for pseudospins and the nearest-neighbor model in zero field is the antiferromagnet studied by Anderson [37].

In the kagome ice problem, two in and one out becomes two down and one up for pseudospins. The Zeeman energy of a kagome plane spin κ , with field along the z axis, can be written $E_\kappa^B = -\sigma_\kappa \tilde{B}$, with $\tilde{B} = -\frac{|\vec{\mu}|B}{3}$ a pseudomagnetic field in the reverse, $-z$ direction. Hence, the three kagome plane spins map onto a kagome antiferromagnet in an external field.

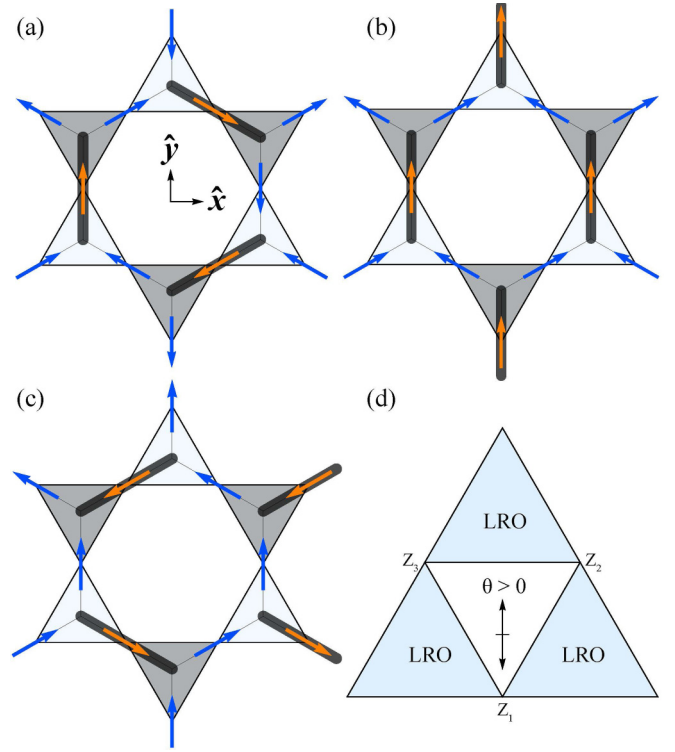


FIG. 2. (a)–(c) Kagome ice, showing the relationship of down spins (orange arrows) and dimers (dark gray rods), where down triangles are shaded gray. (a) Disordered structure. (b) Long-range order induced by a field tilted towards the y direction. (c) Partial order resulting from a tilted field perpendicular to the y direction. (d) Kasteleyn phase diagram, where the central kagome ice state is surrounded by long-range order depending on the sublattice $\kappa = 1, 2, 3$ selected by the tilted field.

The pseudospin correlations can be accessed through the out-of-plane spin components which, as we discuss below, can be measured in the non-spin-flip channel in polarized neutron scattering experiments.

3. Dimer mapping

Moessner and Sondhi's mapping to hard-core dimer configurations on a honeycomb lattice [3] works as follows. The honeycomb lattice and the kagome lattice are a parent/medial pair, with sites of the kagome lattice at the midpoint of the links of the honeycomb lattice [19]. A dimer is placed on a link of the honeycomb lattice located by a kagome site carrying a field-opposing spin, i.e., the outward pointing spin of an up triangle. The kagome sublattice on which the dimer resides is specified by the index κ , as defined above. Figure 2 shows how, if the ice rules are obeyed, there is a single dimer per unit cell and no dimers can touch [27]. The entropic phase of kagome ice is therefore a hard-core dimer liquid which has critical correlations and corresponds to the Coulomb phase for the spins.

As the dimers have no internal energy, the “particle enthalpy” for this system is $\langle \mathcal{H} \rangle = -\sum_\kappa \langle N_\kappa \rangle \mu_\kappa$, with $\langle N_\kappa \rangle$ the mean number of dimers on sublattice κ and μ_κ the relevant chemical potential. The μ_κ correspond to the change in the in-plane component of Zeeman energy of spin κ when it is

flipped to become the out-pointing spin of the triangle:

$$\begin{aligned}\mu_1 &= \left(\frac{4\sqrt{2}|\bar{\mu}|B}{3} \right) \sin\theta \cos\phi, \\ \mu_{2,3} &= - \left(\frac{\sqrt{2}|\bar{\mu}|B}{3} \right) \sin\theta (\cos\phi \pm \sqrt{3}\sin\phi).\end{aligned}\quad (2)$$

These values are defined with respect to a large, positive, and constant term which imposes the constraint that $N_1 + N_2 + N_3 = \frac{N}{3}$, with N the number of spins. The chosen sign giving the favorable placement on the first sublattice with $\mu_1 > 0$ is consistent with the standard conventions of thermodynamics and allows us to define a standard fugacity for dimer placement, $z_\kappa = e^{\mu_\kappa/k_B T}$.

A Kasteleyn transition to dimer alignment on sublattice $\kappa = 1$ occurs when z_1 is equal to the sum of those for the other two sublattices [3,27]: $z_1 = z_2 + z_3$. The transition is from the dimer liquid phase to a dimer solid phase and the phase diagram, illustrated in Fig. 2(d), has threefold symmetry. In terms of the spins, the condition $z_1 = z_2 + z_3$ corresponds to a long-range-ordered ice-rule-obeying state in which the field-opposing spins of the kagome plane are all located on sublattice $\kappa = 1$ [Fig. 2(b)].

4. Phase diagram

To discuss the phase diagram [3], it is convenient for us to define a scale-free parameter

$$\Upsilon(B, T, \theta) \equiv \frac{2\sqrt{2}|\bar{\mu}|B \sin\theta}{\ln 2 \ k_B T} \quad (3)$$

and to determine the value Υ_K that this parameter takes at the Kasteleyn transition. The critical parameter Υ_K will also be a function of the angle ϕ and will play an important role in our future discussion. Moessner and Sondhi previously named this parameter h , but we have chosen Υ to avoid confusion with reciprocal space labeling, i.e., (h, k, l) .

The fugacity relation at the transition is derived in detail in Appendix B and can be written [38]

$$\cosh\left(\frac{\Upsilon_K \sin(\phi) \ln 2}{\sqrt{3}}\right) = 2^{\Upsilon_K \cos(\phi) - 1}. \quad (4)$$

For $\phi = 0$ this is solved for $\Upsilon_K = 1$, giving a surface of Kasteleyn transitions (denoted by subscript K) in the space of (B, T, θ) :

$$k_B T_K = \frac{2\sqrt{2}}{\ln 2} |\bar{\mu}| B_K \sin\theta_K. \quad (5)$$

Usually two parameters will be fixed, typically θ and B (in addition to ϕ), which then uniquely defines the transition point T_K . As the field is rotated in the plane, an iterative solution can be found, with $\Upsilon_K \rightarrow \infty$ for $\phi = \pm 60^\circ$, corresponding to the transition temperature falling to zero.

The characteristic triangular form of the phase diagram with three lines of Kasteleyn transitions separated by discontinuous points thus reflects the symmetry of the kagome plane and rotation of the field between the equivalent $\langle 11\bar{2} \rangle$ and $\langle \bar{1}10 \rangle$ axes, as shown in Fig. 2. The ordered dimer phase, and therefore the saturation magnetization, lies along a local y axis, even for arbitrary ϕ . Hence, for such an arbitrary field

tilt, the induced in-plane magnetization follows the in-plane field direction at high temperature, but as the transition is approached it swings away from the field to order finally along one of the $\langle 11\bar{2} \rangle$ axes.

Given this threefold symmetry, the case $\theta > 0$, $\phi = \pm 60^\circ$ is equivalent to a tilt with $\theta < 0$ and $\phi = 0$. In this situation the dimer/field-opposing spin may occur with equal probability at sites with $\kappa = 2, 3$. No Kasteleyn transition occurs because the degeneracy of the ice-rule states is not fully lifted. Although the entropy is reduced by the tilted field, the resulting state has chains of spins running across the kagome planes that need not be correlated with each other [see Fig. 2(c)]. These are the so-called β chains found when the field is applied along a $\langle 110 \rangle$ -type direction of a spin ice [39,40] or columnar order for dimers (α chains are also present, formed by the apical spins and the uniquely selected kagome sublattice where the spin cannot oppose the field). The dependence on θ can be seen to be asymmetric because in the pyrochlore lattice tilts with $\theta > 0$ represent a tilt of the field toward the bisector of a tetrahedron face, where degeneracy is fully removed [41], while tilts with $\theta < 0$ represent a tilt of the field toward a tetrahedron edge, where degeneracy is only partially removed [39,40].

B. Topological excitations

For a model system, with periodic boundaries, lying within the constrained manifold of states that satisfy the ice rules, the only allowed excitations are correlated spin flips around closed loops. These can be either short loops within the system, which do not change the magnetization, or long loops that span the entire system. The latter, which we call strings, are topological excitations. As a consequence, the magnetization defines the topological sector [42] and both are changed by flipping such strings.

Starting from the ordered state, the only available excitations are the system-spanning strings, which cost an energy that scales linearly with the system size, L . As a result, the system remains completely frozen at low temperature. However, the entropy introduced by a string also scales linearly with L , so their introduction becomes favorable above a singular threshold, which is the Kasteleyn transition. The transition condition (4) follows directly by tracking the free-energy cost δG of introducing a string into the ordered state. As the string passes through each unit cell, the change in Zeeman energy (or dimer number enthalpy) is $\delta\epsilon$ and the entropy creation δs , so $\delta G = L(\delta\epsilon - T\delta s)$, which is zero at the transition. The system can access different string configurations by flipping short loops of spins or dimers. When adding a second string, the two strings cannot pass through the same triangle. Consequently, there is an entropic repulsion between strings and the free-energy cost of adding the second string is slightly greater than the first, ensuring that the transition is continuous rather than discontinuous.

Such strings can be found in other problems of statistical mechanics, mapping onto world lines for hard-core bosons undergoing Bose condensation at the transition [30] or onto directed polymers [43]. In both cases the strings can be thought of as walkers making ballistic progress against the direction of in-plane magnetic order while diffusing along

the axis perpendicular to this direction. For a Kasteleyn transition in higher dimension d the diffusion is in the $(d - 1)$ -dimensional plane perpendicular to the ordering direction. Note that, in spin ice, the strings can in principle meander in three dimensions. In practice, the apical spin is considered to be firmly fixed so that we only consider string and loop excitations in isolated planes and we only simulate a single kagome plane, later returning to the relation with three-dimensional loops in the discussion.

C. Thermodynamics

1. Free energy

As the magnetic ordering occurs along one of the local $(11\bar{2})$ axes, we can restrict the thermodynamic discussion to the case of $\theta > 0$ and $\phi = 0$ without loss of generality. Including a finite in-plane angle ϕ changes the finite-size-scaling properties at the transition, as shown in detail below, but the thermodynamics of the transition is captured by this constrained case. We define $M = \langle \frac{1}{|\bar{\mu}|} \sum_i \bar{\mu}_i \cdot \hat{y} \rangle$, the dimensionless in-plane component of the total magnetic moment, and its conjugate magnetic field variable $H = B|\bar{\mu}| \sin \theta$, the in-plane component of the applied field, in energy units.

All microstates forming the kagome ice manifold have the same internal energy, so the Helmholtz free energy $F(M, T) = -TS(M)$ is purely determined by the system entropy. There are, however interactions, in the form of the hard-core dimer constraints, and these are ultimately responsible for the phase transition, but they do not appear directly in the phenomenology. Phase transitions driven only by entropy are actually not so rare for hard-particle systems [44,45], but two things single out the Kasteleyn transition. The first is that no symmetry, either microscopic or emergent, is broken at the transition, placing the transition outside the usual paradigm in which phase transitions and symmetry breaking in phase space go hand in hand. The second is that the transition occurs for $S = 0$, making it anisotropic, with zero fluctuations on the low-temperature high-field side.

Despite these particularities, a complete thermodynamic description is possible. As in a paramagnet, the two intensive variables H and T collapse into a single thermodynamic variable [38]:

$$\frac{H}{k_B T} = \frac{1}{k_B T} \frac{\partial F}{\partial M} = \frac{-1}{k_B} \frac{\partial S}{\partial M}. \quad (6)$$

In a paramagnet, the entropy approaches zero as the magnetization saturates, but the slope $\frac{\partial S}{\partial M}$ is infinite, precluding a phase transition at finite temperature. Here the entropy is also zero at saturation, but the Kasteleyn phase transition for the finite ratio $(H/k_B T)_K$ ensures that the entropy must go to zero with a finite slope.

2. Landau-style expansion

The asymmetry of the Kasteleyn transition has led previously to a classification lying between first and second order [5], although on the high-entropy side the transition satisfies all the thermodynamic and phenomenological criteria of a second-order transition. The honeycomb lattice dimer problem can be solved exactly with the calculation of the

partition function, all thermodynamic quantities, and correlation functions, but it is useful to develop the phenomenology of the transition through the construction of a Landau-like free energy [43,46].

The Gibbs potential $G^* = F - HM$ can be expanded in powers around the saturated moment M_{\max} . Introducing the dimensionless variable $m = \frac{M_{\max} - M}{N}$ and the dimensionless parameter $\eta = (\frac{H}{k_B T})_K - \frac{H}{k_B T}$, it follows that

$$\frac{G^*}{Nk_B T} = -\eta m + \frac{\alpha_2}{2} m^2 + \frac{\alpha_3}{3} m^3 + \dots - \frac{\mu_0 H M_{\max}}{Nk_B T}, \quad (7)$$

where α_i are the parameters of the expansion of G^* in m . Minimizing with respect to m , the leading term of the Gibbs free energy is $G \sim -\eta^{1+\beta}$, with $\beta = 1$ at this mean field level, while the exact solution [27] yields $\beta = \frac{1}{2}$ [3]. The entropy $S = -\frac{\partial G}{\partial T} \sim \eta^\beta \sim m$ indeed scales linearly with M near the transition, consistent with the finite value for $(H/k_B T)_K$.

The magnetization is singular around its maximum value $m \sim \eta^\beta$ and as there is a single intensive thermodynamic variable, the critical exponents for the susceptibility $(-\frac{\partial^2 G}{\partial T^2})$ and specific heat $(-T \frac{\partial^2 G}{\partial T^2})$, γ and α , are equal. As a consequence, the Rushbrooke scaling relation $\alpha + 2\beta + \gamma = 2$ reduces to $\beta + \gamma = 1$. This means that the one scaling dimension $\Delta = \gamma + \beta$ is unity, which excludes anomalous scaling, ensuring Gaussian exponents for dimensions below the upper critical dimension [47].

The singular free energy can be equated to the inverse correlation volume $G \sim \xi_x^{-(d-1)} \xi_y^{-1}$, where $\xi_y \sim \eta^{-\nu_y}$ and $\xi_x \sim \eta^{-\nu_x}$ are the diverging correlation lengths parallel and perpendicular to the ordering direction, respectively. From this the modified hyperscaling relation $1 + \beta = (d - 1)\nu_x + \nu_y$ follows [47]. From the insertion of a single string with its ballistic and diffusive nature parallel and perpendicular to the ordering direction, respectively, we can anticipate that $\nu_y = 1$ and $\nu_x = \frac{1}{2}$, consistent with the absence of an anomalous scaling dimension and with the exact results in two dimensions. Putting the mean field value $\beta = 1$ into the hyperscaling relation gives an upper critical dimension of $d = 3$ [30,43], so the two-dimensional problem is outside the mean field regime. Indeed, the exact result yields $\beta = \frac{1}{2}$ and $\gamma = \frac{1}{2}$.

Hence, from this analysis one can conclude that the singular part of the free energy satisfies the scaling and hyperscaling relations for a critical point for a one-parameter system.

D. Correlation functions

From the analytic solutions for the correlation function [3], one finds the expressions for the correlation lengths

$$\xi_x^{-1} = \arcsin \sqrt{1 - 4^{\gamma-1}}, \quad (8a)$$

$$\xi_y^{-1} = \xi_x^{-1} \frac{2^{2-\gamma}}{3} \sqrt{1 - 4^{\gamma-1}}, \quad (8b)$$

which near the transition take the power-law forms discussed above, with $\nu_x = \frac{1}{2}$ and $\nu_y = 1$, as found by expanding Eq. (8a) in η . Unusually, the development of diverging correlation lengths does not signal the onset of power-law correlations. In the Coulomb phase, with zero tilted field, both spin and dimer correlation functions are already of dipolar

form with, in two dimensions, correlations falling as $\sim 1/r^2$ at large distance, giving characteristic logarithmic divergences with system size, for the structure factors. The growing correlation lengths introduce an anisotropy to the correlation functions with in-plane distance r replaced by an effective scale

$$r' = \sqrt{x^2 + \left(\frac{\xi_y}{\xi_x}\right)^2 y^2}. \quad (9)$$

Structure factors for both pseudospins and real spins can be accessed by polarized neutron scattering (discussed below). As the transition is approached, the developing anisotropy causes peaks in both structure factors to drift towards the Brillouin zone center and to sharpen, arriving there as the transition is reached. Kagome ice therefore has field-tunable critical correlations, with the drift determining the ratio of the correlation lengths [3].

III. NUMERICAL SIMULATIONS

A. Details of simulations

Given the constraints discussed above, for our simulations we were able to limit the Hamiltonian of two-dimensional kagome ice to the Zeeman energy term

$$\mathcal{H} = -\vec{H} \cdot \sum_i \vec{S}_i. \quad (10)$$

Here \vec{S}_i is a dimensionless vector of length $S_{\perp} = \frac{2\sqrt{2}}{3}$, describing the component of the magnetic moment lying in the x - y plane, $\vec{\mu}_i = |\vec{\mu}| \vec{S}_i + \mu_i^z \hat{z}$, and \vec{H} is the field component in the plane for arbitrary ϕ , again expressed in energy units.

This system was updated using a worm algorithm, full details of which are given in Appendix C. In the following, we report simulations of diffuse neutron scattering from the magnetic moments with both in-plane and z components. In a polarized neutron scattering experiment, the in-plane spin components will be observed in the spin flip (SF) channel, while the z components, corresponding to the pseudospin variables, will be observed in the non-spin-flip (NSF) channel.

The majority of our simulations were carried out on a system of 8112 spins ($L \times L$ kagome unit cells with $L = 52$) with periodic boundary conditions. For finite-size-scaling analysis the simulation sizes were extended to 99 856 spins ($L = 316$). At the start of the simulation, the system was placed in an ordered state at zero temperature [as illustrated in Fig. 2(b)] and then evolved upward in temperature under constant field. The diffuse scattering maps were each generated from 100 independent spin configurations.

B. Simulated Kasteleyn transition

1. Neutron scattering map at $\theta = \phi = 0$

We first examine the manifestations of the Kasteleyn transition in the diffuse neutron scattering structure factor as predicted in Ref. [3]. In the reciprocal space of the pyrochlore structure, the scattering plane that is perpendicular to the applied field direction is spanned by the vectors $(\bar{h}, h, 0)$ and $(\bar{k}, \bar{k}, 2k)$. For convenience, we refer to the

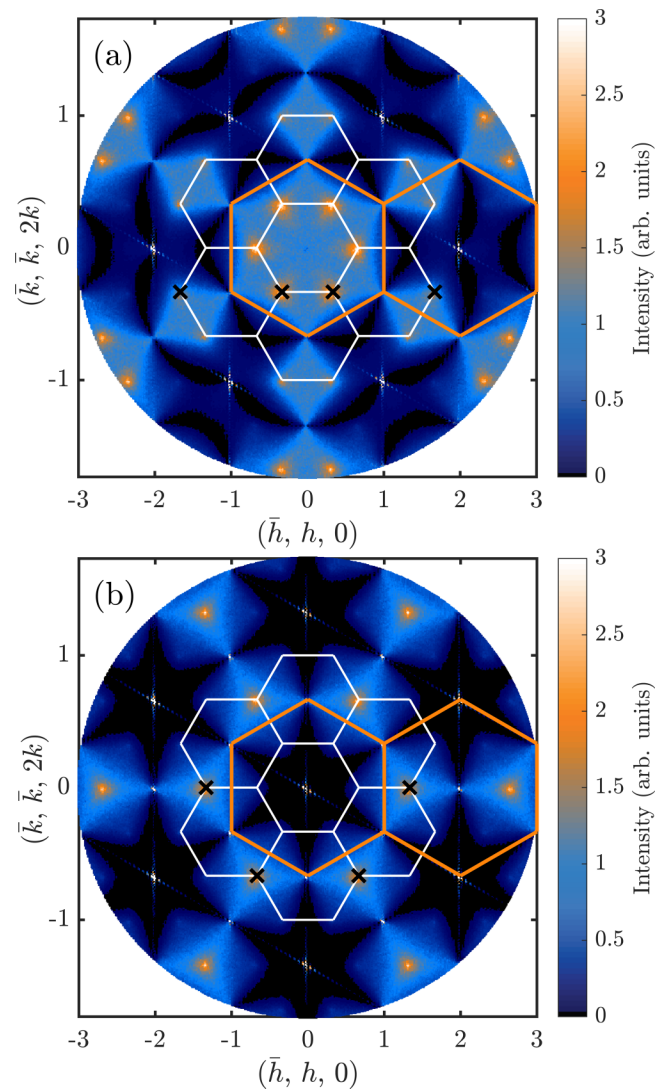


FIG. 3. Differential scattering cross section of kagome ice with $\theta = 0$ and $\phi = 0$ in the (a) SF and (b) NSF channels. The sixfold symmetry of the kagome plane is notable and can be seen in the precise positioning of diffuse peaks on the kagome zone corners (white hexagons; orange hexagons are pyrochlore zones). Crosses mark peaks whose positions were tracked and are discussed in the text.

two-dimensional coordinates (h, k) of the point on the scattering plane $h(\bar{1}, 1, 0) + k(\bar{1}, \bar{1}, 2)$.

Figure 3 illustrates the scattering patterns for $\theta = 0$. These are sixfold symmetric pinch point patterns characteristic of the kagome ice Coulomb phase. They include sharp Bragg peaks at the $(2,0)$ points signaling the partial all-in-all-out order [32]. As the tilt is applied, the in-plane field lowers this symmetry to twofold with the development of arms of more intense scattering either side of the ordering direction [48]. In Fig. 4 we show the general features of the pseudospin (NSF) and noncollinear spin (SF) structure factors and an example of their evolution in tilted field with $\theta > 0$ and $\phi = 0$.

Our numerical results are consistent with experiment (discussed below) but show detailed differences from the analytical predictions of Moessner and Sondhi [3]. In our

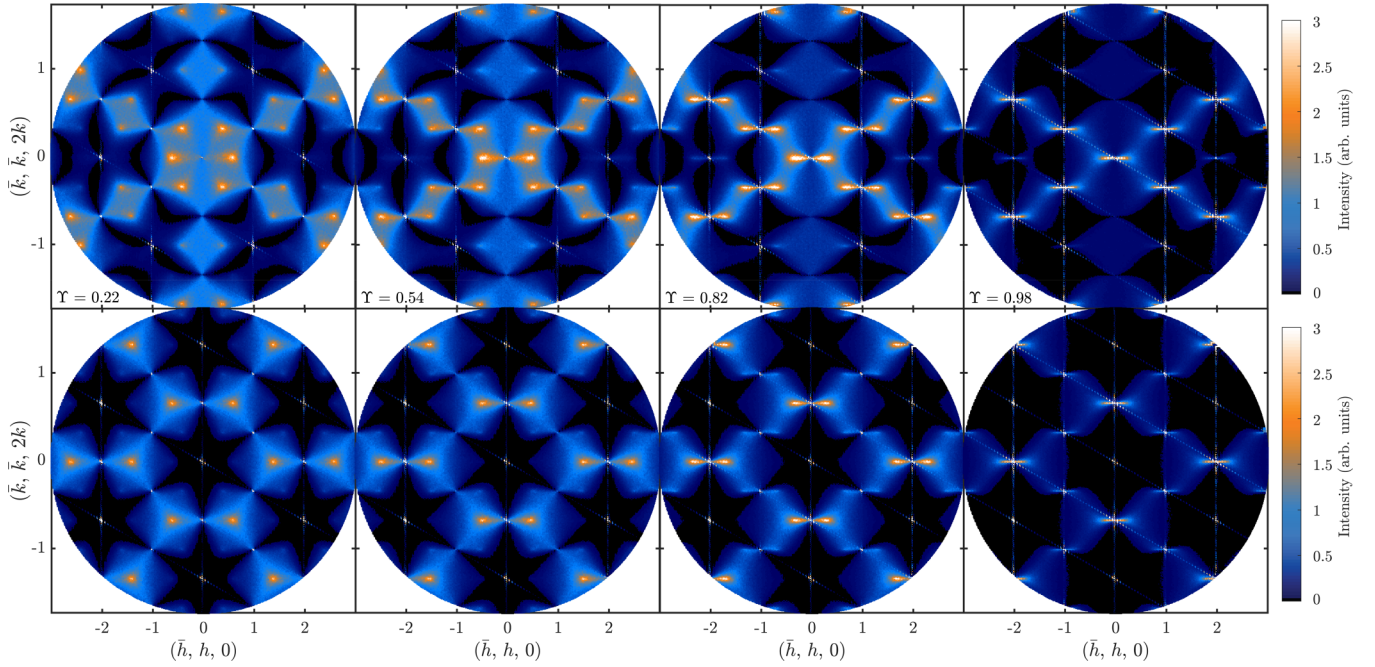


FIG. 4. Simulated evolution of the diffuse neutron scattering as the Kasteleyn transition is approached. The top row of panels shows the scattering in the spin-flip channel and the bottom row shows the non-spin-flip channel as a function of the parameter $\Upsilon(B, T, \theta)$ in Eq. (3). When Υ is small, the breaking of the sixfold symmetry of the kagome ice scattering patterns to twofold is only just apparent, but as $\Upsilon \rightarrow \Upsilon_K = 1$ it becomes increasingly evident. As Υ increases, diffuse peaks (orange) in both channels start close to Brillouin zone corners of the kagome lattice and drift in the x direction toward the pinch points at kagome lattice Brillouin zone centers.

pseudospin or NSF structure factor, a single peak appears at $(\frac{4}{3}, 0)$, with intensity falling to zero for a group of three points located symmetrically around $(1, 0)$ and including $(\frac{2}{3}, 0)$. In Ref. [3] there is an inverse pattern with three peaks appearing at these points and zero intensity at the position of our peak (see Ref. [38] for a detailed comparison).

2. Drift of peaks at $\theta \neq 0$ and $\phi = 0$

Both the simulated spin and pseudospin structure factors confirm that the diffuse peaks drift [3], with increasing field tilt, from their initial locations close to the Brillouin zone boundaries, towards the pinch points at the zone center. The intensity of the peaks (not illustrated here; see Ref. [38]) is further confirmed to depend logarithmically on the size of the system as predicted [3], while the Bragg peak intensities scale linearly with the system size. The peak shape (Fig. 5) is also predicted to be logarithmic [3] and is well described by back-to-back logarithmic decay functions, which affords a superior description to a single Lorentzian [although the difference turns out to be less significant in experiment; see Fig. 5(b)]. The pseudospin structure factor corresponds to that of an Ising antiferromagnet on the kagome lattice, constrained to the two-up–one-down sector of states by an external field.

In Fig. 6 we show the inverse correlation lengths extracted by tracking the position of the logarithmic peak at $(\frac{4}{3}, 0)$ in the NSF channel (i.e. the pseudospin correlation function). The peak positions are extracted from the simulated scattering pattern by applying the same peak tracking algorithm that we apply to the experimental data and describe in full in Appendix E. As can be seen in Fig. 4, the evolution of

this peak with field tilt ($\theta > 0, \phi = 0$) is along the $(\bar{h}, h, 0)$ axis towards the kagome zone center at $(2, 0)$, which gives a direct measure of ξ_x^{-1} as proposed in Ref. [3]. No independent measure for ξ_y^{-1} was described, but ξ_y^{-1} can be extracted from the measurement of ξ_x^{-1} through Eq. (8a). The corresponding data are also included in Fig. 6, where it can be seen that the numerics track the analytic calculation with high precision right up to the Kasteleyn transition, despite the peak appearing at a different reciprocal space position [3]. Usually inverse correlation lengths are measured using the width of features in reciprocal space and this method can in principle be used here. In Fig. 7 we show the evolution of the width of the logarithmic peak along both $(\bar{h}, h, 0)$ and $(\bar{k}, \bar{k}, 2k)$. Although the data are noisy, an evolution scaling like ξ_x^{-1} can be identified in both cases.

C. Exploration of general tilt $\phi \neq 0$

In this section, we identify some topological consequences of general tilt $\phi \neq 0$.

1. Scattering function

Finite ϕ acts to further lower the symmetry for dimer placement in the kagome plane and hence further lowers the symmetry of the in-plane scattering function. The effects of this reduced symmetry are shown in Fig. 8, where the twofold symmetry observed for $\phi = 0$, which is visible in Fig. 4, is reduced, with the emergence of an arm of intense scattering on each side of the scattering plane. However, features still

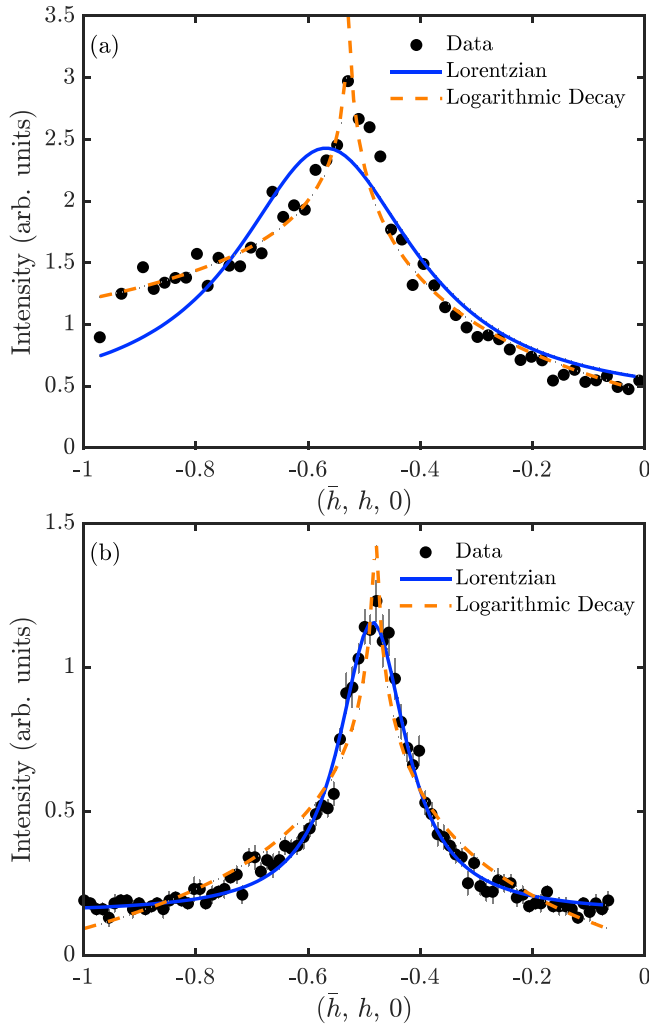


FIG. 5. (a) Simulated logarithmic peak in the SF channel ($\Upsilon = 0.54$) at approximately $(-\frac{2}{3}, -\frac{1}{3})$ (see Fig. 4). We show a comparison of fits of two logarithmic decay functions [$a \log(b - x) + c$] that intersect at infinity at the peak maximum with a fit to a single Lorentzian. (b) For comparison we include the experimental data of Fig. 14 (0.75 K and 1 T), where this peak is marked by crosses. The estimated Υ for the experimental data is 0.45 for $\theta = 0.7^\circ$. The discrimination between logarithmic and Lorentzian is not so clear in experiment.

drift as the system evolves towards the Kasteleyn transition, as shown in Fig. 9.

2. Finite-size scaling of the susceptibility

Rotating the tilted field in the plane has spectacular consequences for the string insertion close to the transition. In Fig. 10 we show a snapshot of the in-plane spins for $\phi = 50^\circ$ in which we highlight the first string placed in the system. The string progresses through the system propagating in a mean direction $\phi' < 0$ which minimizes the unfavorable Zeeman energy (see Appendix C). This makes it incompatible with the periodic boundaries, forcing it to make multiple loops of the system before closing on itself. The multiple passages are characterized by a cut variable Y , as shown in the figure.

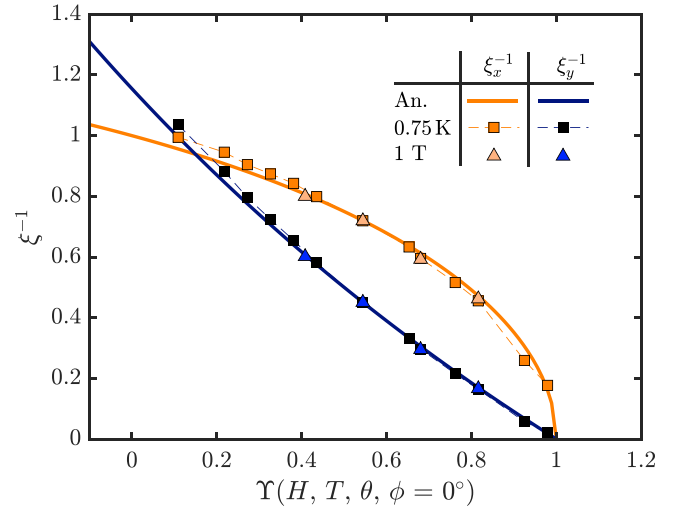


FIG. 6. Simulated inverse correlation length ξ_x^{-1} obtained by tracking the position of the logarithmic peak at $(\frac{4}{3}, 0)$ (when $\Upsilon = 0$) in the Monte Carlo simulation of the NSF channel, as well as ξ_y^{-1} obtained from it, compared with the analytical predictions of Ref. [3] (labeled “An.”).

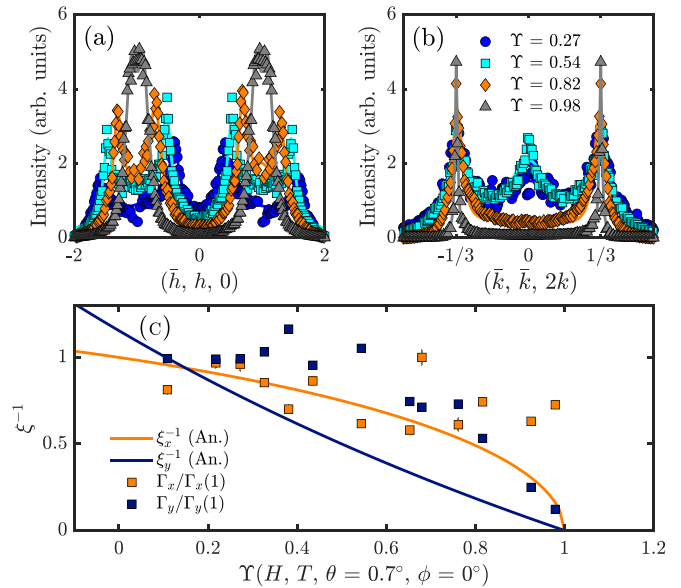


FIG. 7. (a) Cuts through simulated data ($\phi = 0$) at several different values of Υ_K approaching the Kasteleyn transition. The cuts are perpendicular to $(\bar{k}, \bar{k}, 2k)$, at the average peak center for each of the four logarithmic peaks (which are fitted by four Lorentzians). (b) Cuts of simulated data at the same values of Υ_K at the location on $(\bar{h}, h, 0)$ of the average peak centers for two peaks that overlap with the experimental data. The central peak at small Υ_K is another logarithmic peak that drifts towards a different kagome ice Brillouin zone center not found on this cut along $(\bar{h}, h, 0)$. (c) The average width Γ of the four fitted Lorentzians in (a) as a function of Υ_K for $(\bar{h}, h, 0)$ [cuts at constant $(\bar{k}, \bar{k}, 2k)$] and $(\bar{k}, \bar{k}, 2k)$ [cuts at constant $(\bar{h}, h, 0)$], showing that the widths of the logarithmic peaks cut in either direction resemble ξ_x rather than ξ_y .

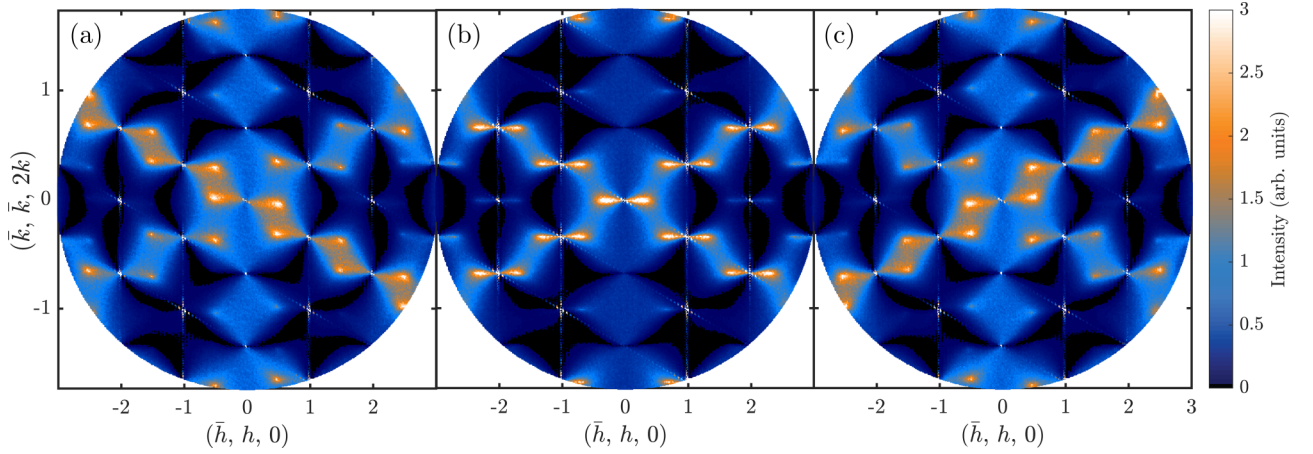


FIG. 8. Simulated spin-flip neutron scattering structure factor with angles (a) $\phi = -50^\circ$, (b) $\phi = 0^\circ$, and (c) $\phi = 50^\circ$ corresponding to $\Upsilon/\Upsilon_K = 0.42$, (b) $\Upsilon/\Upsilon_K = 0.82$, and (c) $\Upsilon/\Upsilon_K = 0.42$ (in the experimental system this would correspond to 0.75 K and 1.5 T for all values of ϕ).

This approach to incommensurability has a dramatic effect on the finite-size-scaling properties of the susceptibility χ , which following the finite-size-scaling hypothesis can be written, close to the transition in the form

$$\chi = \eta^{-\gamma} \mathcal{G}\left(\frac{\xi_x}{RL}, \frac{\xi_y}{L}\right), \quad (11)$$

where \mathcal{G} is a scaling function and $R = (\frac{1}{\Upsilon})^{\nu_y/\nu_x}$ is an incommensurability function similar to the shape function studied in the context of directed polymers [43]. When $\phi = 0$, as $\xi_y \gg \xi_x$, the scaling function should be dominated by the ballistic propagation of the strings in the y direction and consequently depend on the single variable ξ_y/L . This is achieved by setting $Y = 0$ ($R = \infty$).

In an incommensurate situation, as the string length becomes indeterminate, the diffusive evolution of the string in the perpendicular plane, with associated correlation length ξ_x , should dominate the finite-size scaling. As the incommensurability factor evolves from $Y = 0$ ($R = \infty$) to $Y = \infty$ ($R = 0$), the scaling function should evolve between these regimes. For any finite R , \mathcal{G} should ultimately cross over to the ballistic

case, with the crossover region scaling closer and closer to the transition as R increases.

In consequence, different finite-size-scaling predictions emerge in the two limits. Identifying $\eta^{-\gamma} = \xi_y^{\gamma/\nu_y}$ in the ballistic limit and $\eta^{-\gamma}$ as ξ_x^{γ/ν_x} in the incommensurate limit, the scaling hypothesis can be rewritten

$$\begin{aligned} \chi_B &= L^{\gamma/\nu_y} \mathcal{G}_B\left(\frac{\xi_y}{L}\right), \\ \chi_I &= L^{\gamma/\nu_x} \mathcal{G}_I\left(\frac{\xi_x}{L}\right), \end{aligned} \quad (12)$$

where $\mathcal{G}_B(\xi_y/L)$ and $\mathcal{G}_I(\xi_x/L)$ are new scaling functions.

This phenomenology is confirmed by simulation in Figs. 11 and 12. In Fig. 11 we show the susceptibility near the transition for $\phi = 0$ and for different system sizes. The divergence of the susceptibility at the transition is cut off by the finite size of the sample, as shown in Fig. 11(a). The finite-size scaling is tested in Fig. 11(b), where, setting $\gamma = \frac{1}{2}$ and $\nu_y = 1$, we plot $\chi L^{-1/2}$ against $(T - T_K)L$ at fixed H , finding an excellent data collapse corresponding to the ballistic limit.

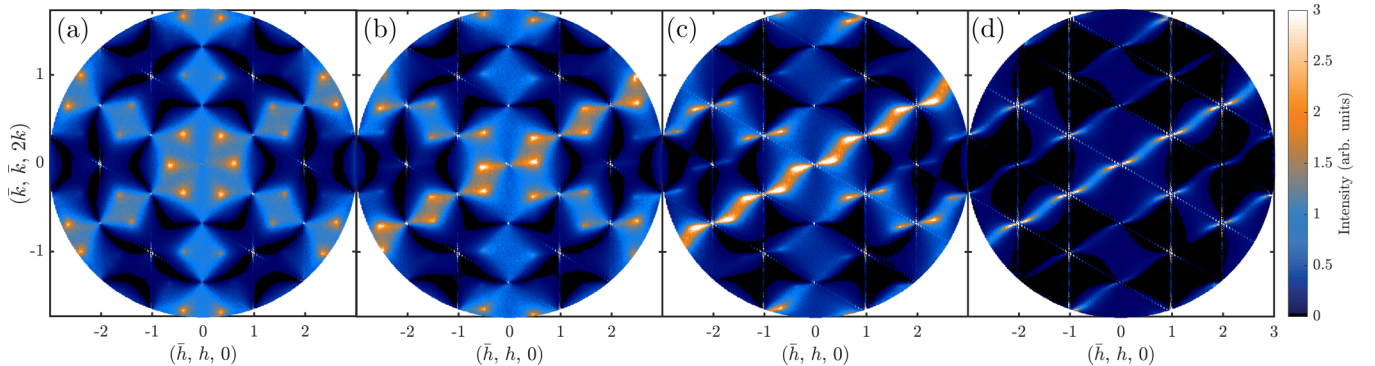


FIG. 9. Simulated spin-flip neutron scattering structure factor with an angle $\phi = 50^\circ$, as a function of Υ/Υ_K [Eq. (4)] at (a) $\Upsilon/\Upsilon_K = 0.11$, (b) $\Upsilon/\Upsilon_K = 0.42$, (c) $\Upsilon/\Upsilon_K = 0.76$, and (d) $\Upsilon/\Upsilon_K = 0.99$ (in the experimental system this would correspond to 0.75 K and 0.4, 1.5, 2.7, and 3.5 T, respectively).

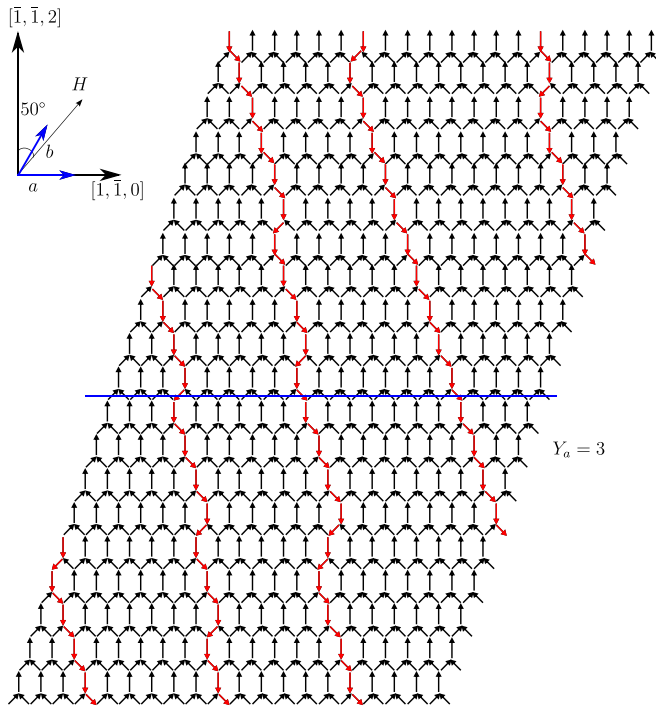


FIG. 10. Snapshot of the kagome ice lattice taken from a simulation at $T = T_K$ and $\phi = 50^\circ$. The lattice contains a single string (highlighted in red) which winds around the lattice through the periodic boundary conditions until it closes on itself. This snapshot shows the loop forming in a direction that is approximately perpendicular to the field direction as this minimizes its unfavorable Zeeman interaction. The blue line parallel to the lattice vector is a trajectory for calculating a cut number which records the number of times a string is encountered in that direction.

In Fig. 12 we show finite-size scaling for data with $\phi = 20^\circ$. In Fig. 12(a) we show that the ballistic scaling fails to give data collapse. However, in Fig. 12(b) we test the incommensurate scaling by setting $\gamma = \frac{1}{2}$ and $\nu_x = \frac{1}{2}$ and plotting χL^{-1} against $(T - T_K)L^2$ at fixed H , finding an encouraging collapse of the numerical data. Although the simulation is quite challenging and the data remain noisy, it seems that we have clear evidence of the crossover between the two scaling limits [43].

In the first instance the ballistic universal function shows a broad single-peaked function, while in the incommensurate case two peaks are visible. This is because, in the ballistic case, the scaling is many body, with many simultaneous strings present in the large- L limit. In the incommensurate case, despite reaching the scaling limit, one sees the individual effect of adding one string at a time. Our data show the effect of adding a first string and then a second, but more extensive simulations should reveal a comb of single-string peaks stretching out from the transition [43].

Finally, in Fig. 13 we show the equivalent of Fig. 6 for $\phi = 20^\circ$ and $\phi = 50^\circ$, the evolution of the correlation lengths with Υ_K . We see that, despite the radical change in finite-size scaling of the susceptibility as ϕ increases from zero, the behavior of the correlation lengths as a function Υ_K is independent of the finite-size-scaling regime reached.

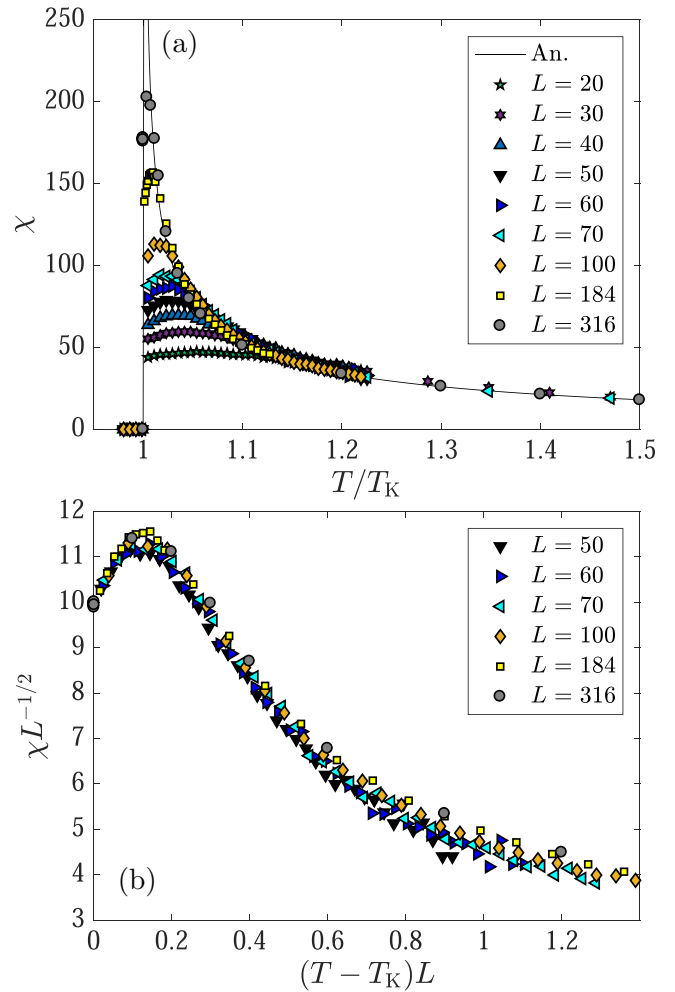


FIG. 11. (a) Simulated susceptibility of the kagome ice lattice with the field at an angle $\phi = 0^\circ$ as a function of lattice size. Also shown is analytical susceptibility in the thermodynamic limit (labeled “An.”) [3]. (b) Same data as in (a) plotted as a function of scaling variables in the ballistic limit. The collapse of the data over a large range of lattice sizes validates the ballistic scaling controlled by the correlation length parallel to the direction of the ordered moment.

IV. EXPERIMENT

A. Method

A large single crystal of $\text{Ho}_2\text{Ti}_2\text{O}_7$ was grown by the floating zone method. The crystal approximated a long cylinder ($d \approx 7$ mm, $l \approx 60$ mm) with a visible (1, 1, 1)-type facet running the length of the boule. It was previously used to measure diffuse scattering in zero field [20]. To ensure a precise alignment, a face perpendicular to the longest $\langle 111 \rangle$ direction was cut so that when the crystal rests on the cut face, the $(\bar{h}, h, 0) - (\bar{k}, \bar{k}, 2k)$ plane lies in the horizontal scattering plane of a neutron spectrometer, with the [111] direction vertical. The long axis of the crystal boule makes an angle of 26° with the vertical direction and is coplanar with the [111] and $(\bar{k}, \bar{k}, 2k)$ directions (Fig. 15).

The crystal was held in a copper clamp running the length of the boule, attached to a block with cutouts that allow two adjustable orthogonal tilts and a continuous metallic path from

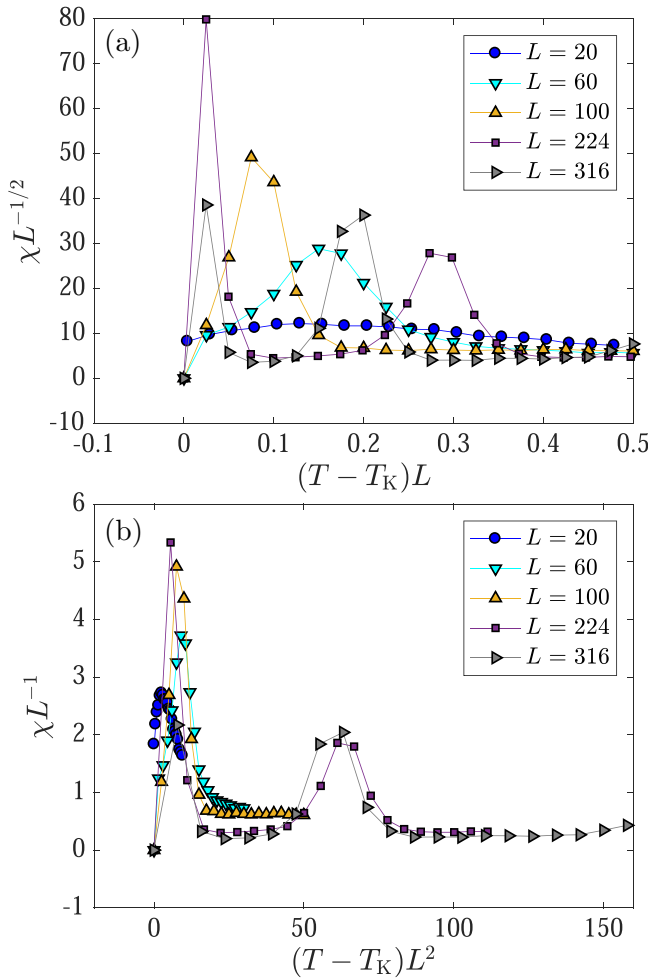


FIG. 12. Simulated finite-size-scaling function applied at an angle of $\phi = 20^\circ$. (a) Data are plotted as a function of scaling variables in the ballistic limit. (b) Scaling variables for the incommensurate limit are used. A better fit is clearly obtained in (b), illustrating the crossover with ϕ between the two scaling regimes governed by the correlation lengths parallel and perpendicular to the direction of the ordered moment.

the sample clamp to the mixing chamber of the dilution fridge. Neutron Laue diffraction measurements were used to refine the alignment and showed that the crystal was mounted with $\theta \lesssim 0.1^\circ$ and $\phi \lesssim 0.2^\circ$ and the adjustable tilts were locked by opposing screws to prevent any movement of the sample by the applied field. The sample was mounted in a dilution refrigerator insert, which itself was mounted in a 2.5 T vertical field cryomagnet. The cryomagnet plus refrigerator insert and crystal were placed in the polarized neutron diffuse scattering spectrometer D7 at the Institut Laue Langevin (Grenoble, France) [49] with the $(\bar{k}, \bar{k}, 2k)$ defined by Laue diffraction approximately antialigned with the incident beam (i.e., with the tilted crystal boule approximately coplanar with the incident beam and vertical field and [111] directions).

Diffuse scattering structure factors were measured in the $(\bar{h}, h, 0)$ - $(\bar{k}, \bar{k}, 2k)$ scattering plane using neutrons with wavelength $\lambda = 4.8 \text{ \AA}$. The flipper currents were optimized using a 40-mm-long “quartz” (amorphous silica) sample (matching the sample height) for selected fields from 0.1 to 2.5 T. The

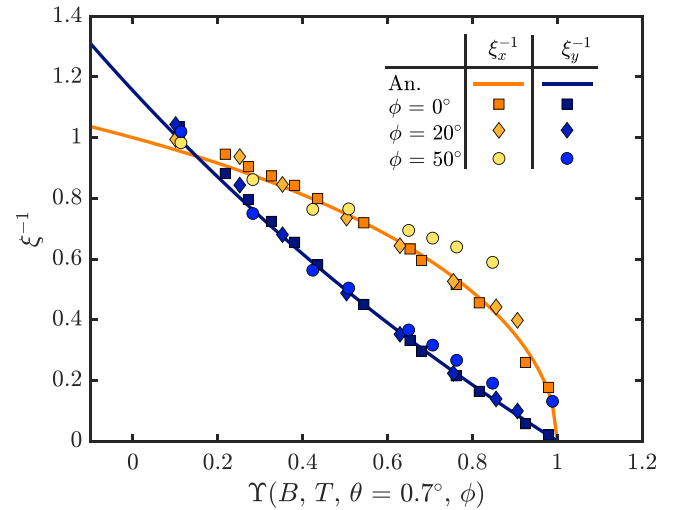


FIG. 13. Simulated scaling of the correlation lengths in systems with $\phi = 0, 20$, and 50° . (compare with Fig. 6, where $\phi = 0$), as obtained by tracking the position of the peak at $(\frac{4}{3}, 0)$ (when $\Upsilon = 0$) in the Monte Carlo simulation of the NSF channel, compared with the analytical predictions of Ref. [3] (labeled “An.”).

cryomagnet provides the guide field at the sample position and only z (NSF) and z' (SF) channels can be measured. Empty sample holder measurements were used to subtract field-independent background scattering. Measurements of the quartz sample (for each field) and a vanadium cylinder (at 0.1 T) were used to calibrate polarization efficiency and detector efficiency, respectively.

Maps of the structure factor were made by measuring intensity in the z and z' channels while rotating the crystal about the vertical axis, also called an ω scan. The data were transformed from the ω - 2θ frame to q_x - q_y , and an additional arbitrary offset angle ω_0 was used to rotate the scattering map to bring particular features to special values of (q_x, q_y) . Usually this corresponded to placing two orthogonal Bragg peaks on q_x and q_y axes so that the scattering plane could be identified by its symmetry axes. In this case, we also used ω_0 to place a specific feature such as a pinch point parallel or perpendicular to q_x or q_y to facilitate cutting through the feature, and by relating the initial crystal orientation with the ω angles at which Bragg peaks were observed, we could identify which of the $(\bar{k}, \bar{k}, 2k)$ axes were associated with the real shape of the crystal.

B. Results

1. Field alignment

Although the crystal axes were initially aligned precisely with the applied field, comparison of the recorded data with simulation immediately suggests that the actual field within the sample was tilted. That is, the diffuse scattering data measured in the $(\bar{h}, h, 0)$ - $(\bar{k}, \bar{k}, 2k)$ plane have distinctive features, characteristic of the kagome ice phase in a tilted field. As can be seen in Fig. 14, the symmetry of the diffuse scattering in the SF and NSF channels is reduced from sixfold to approximately twofold. This is particularly pronounced in the SF channel, where the scattering is stronger, and the reduced

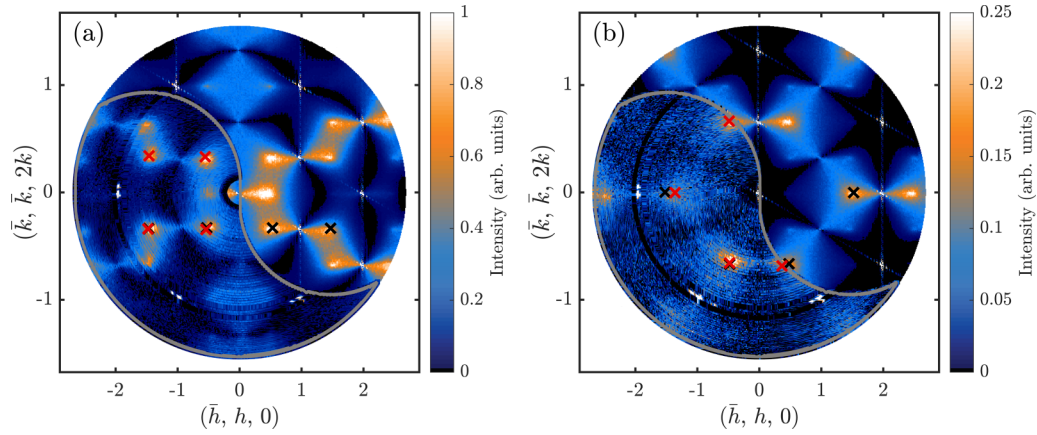


FIG. 14. Experimental data for (a) the SF channel and (b) the NSF channel measured at 0.75 K and 1.0 T, compared with Monte Carlo simulations of kagome ice at $\Upsilon_K = 0.54$ ($\phi = 0$). The experimental data are in the lower left quadrant of each panel and the results from MC simulation are in the upper right. Crosses indicate the peak positions found by the peak tracking algorithm.

symmetry can be clearly seen by comparing to a Monte Carlo simulation of kagome ice with a field tilt, $\theta > 0$, $\phi = 0$. Quantitative comparisons with theory and simulation discussed below suggest that $\theta \approx 0.7^\circ$ (and $\phi \approx 0$). Note that while this crystal showed positive tilt, a previously studied crystal of a different shape [14] showed negative tilt of similar magnitude.

Given the precise alignment of the crystal, an obvious cause of the tilted field is the large demagnetizing effects in spin ice [50]. If the sample is approximated as an ellipsoid whose unique axis is misaligned with the applied field, then the internal field will be uniform but not parallel to the applied field. As noted by Morris *et al.* [51], the large, anisotropic shaped crystals of spin ice typically used in neutron scattering typically suffer from a significant misalignment of the internal field and applied field. The exceptionally large demagnetizing fields of spin ice are well established, having been much discussed with respect to experimental corrections [52] and also as exemplifying departures from the usual textbook theory

of demagnetizing factor [53,54]. The elongated shape of our sample and its tilted relation to the scattering plane therefore provides a convincing explanation of why the internal field is tilted and this may be safely assumed going forward.

The ω angles at which the $(\bar{2}, 2, 0)$ reflections were observed tell us that the uniquely selected $(k, k, \bar{2}k)$ direction is not the one that is coplanar with the maximum tilt of the crystal boule, as would be the case for a weakly magnetized sample, but is instead at 60° to this direction. We have chosen ω_0 to place the uniquely selected direction parallel to q_y . Figure 15 shows its relation to the crystal in direct space.

2. Correlation functions

As discussed above, the SF channel measures in-plane spin components and hence in-plane kagome ice correlations, while the NSF channel detects out-of-plane components and hence correlations of the pseudospins: a model kagome Ising antiferromagnet. The latter cross section is much weaker, because the major part of the total $10 \mu_B$ moment ($\frac{8}{9}$) contributes to the scattering process in the spin-flip channel, while only a smaller projection ($\frac{1}{9}$) contributes to the NSF channel. However, a general comparison with simulations in Fig. 14 clearly shows the different forms of the scattering and that descriptions in terms of either correlation function are warranted.

Figure 16 compares the SF scattering under different applied fields at a fixed temperature of 0.75 K. It shows that features in the diffuse scattering clearly drift across the scattering plane as the field is changed [3], as was found with a more limited data set in Ref. [14]. At fixed field, the features also move as a function of temperature. However, we see that for $T \approx 0.6$ K, the scattering pattern becomes independent of temperature and field within the kagome ice plateau.

3. Aspects not addressed by theory

The experimental data give access to two more aspects of kagome ice that are not addressed by the theory or the simulations described above: the behavior of the pinch points and the approach to plateau termination.

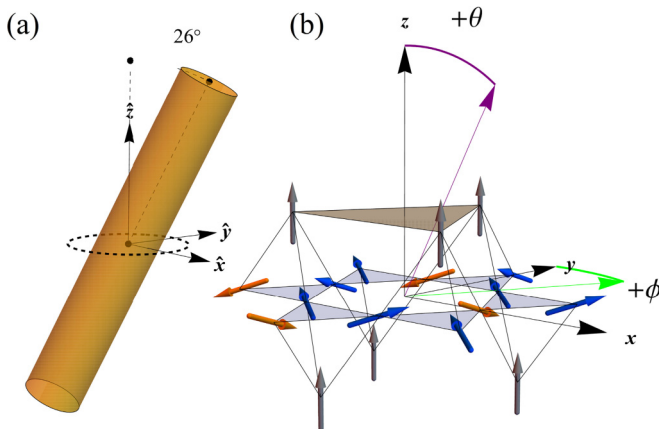


FIG. 15. (a) Schematic of the crystal in direct space showing the axis vectors $x = [\bar{1}10]$, $y = [\bar{1}\bar{1}2]$, and $z = [111]$. (b) Lattice in the same orientation, with the angles θ and ϕ defined in purple and green, respectively.

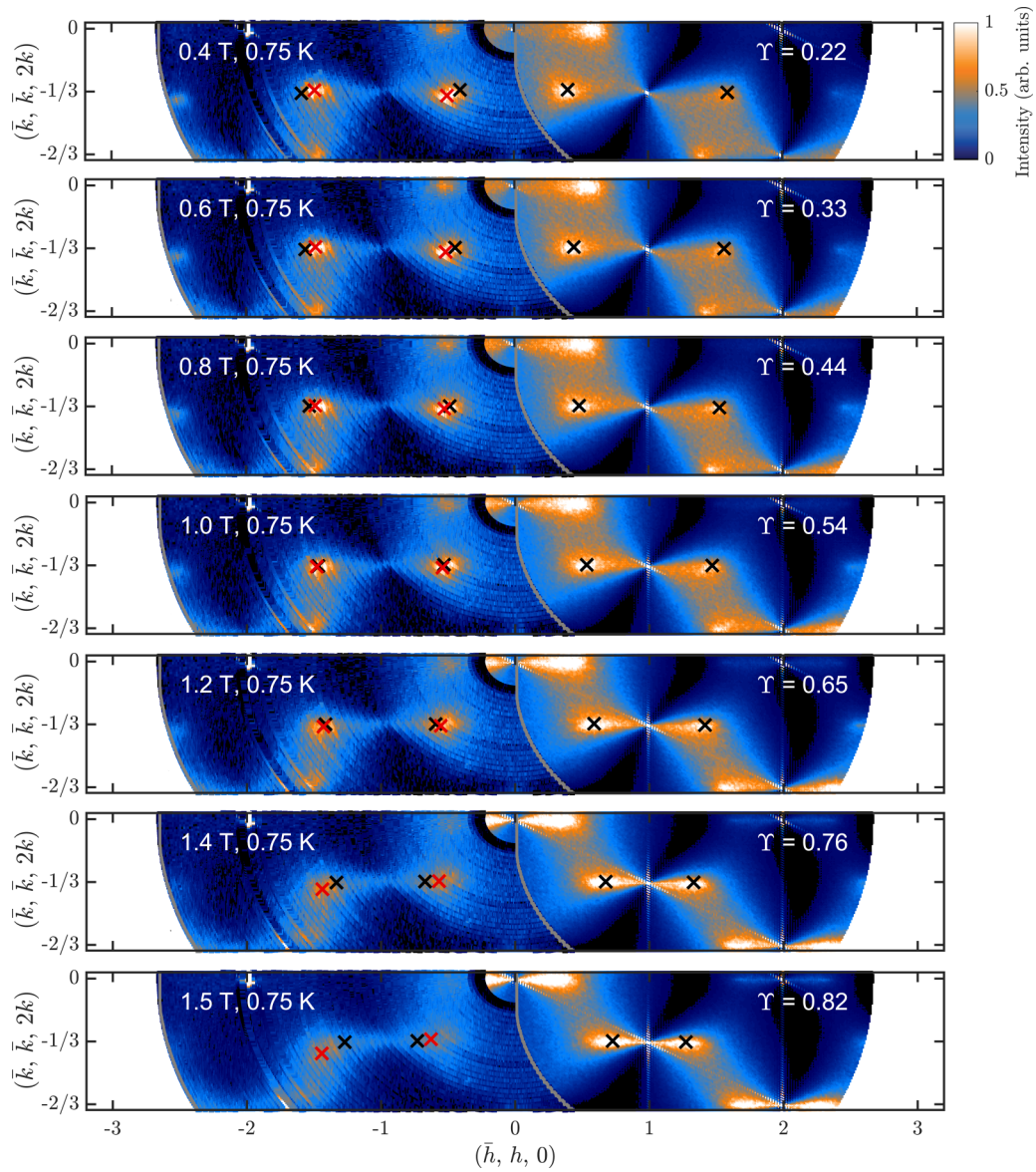


FIG. 16. Diffuse scattering in the SF channel (i.e., due to kagome ice spin components) as a function of applied field at a fixed temperature of 0.75 K. Experimental data are shown in the left part of each panel and Monte Carlo simulations in the right part of each panel. The simulations are carried out at the value of Υ_K determined by these field and temperature values that best match θ . Crosses show the experimental (red) and simulated (black) peak positions.

Referring to Fig. 17(a), we see that, within the kagome ice plateau, at a constant applied field of 1 T, the pinch points sharpen as the temperature decreases to $T \gtrsim 0.6$ K, and below this temperature they remain of constant width, as with other parts of the diffuse scattering mentioned above. At fixed temperature (0.75 K), the pinch points are similarly sharp within the kagome ice plateau ($0.4 < H < 1.4$ T), but as the plateau termination field approaches, they begin to broaden [Fig. 17(b)].

C. Scaling

From tracking peak locations in the diffuse neutron scattering patterns and fitting the wave vectors and intensities, we can reproduce the normalized inverse correlations ξ_x^{-1} and ξ_y^{-1} (see Secs. IID and IIIB2). The location of a pair of diffuse

scattering peaks on either side of the pinch point at $(\bar{1}, \frac{1}{3})$, as indicated on Figs. 14 and 16 by crosses [i.e., at $(\frac{2}{3}, \frac{1}{3})$ and $(\frac{4}{3}, \frac{1}{3})$ in Figs. 14 and 16], was extracted with the peak tracking algorithm described in Appendix E. The reciprocal space distance from each diffuse peak to the kagome Brillouin zone center in $(\bar{h}, h, 0)$ (as denoted by the white hexagons in Figs. 14 and 16) was averaged to produce the inverse correlation lengths ξ_x^{-1} and ξ_y^{-1} through application of Eq. (8a).

The results are shown in Fig. 18, where they can be compared with the analytic results with $\nu_x = \frac{1}{2}$ and $\nu_y = 1$. We find qualitative agreement between theory and experiment for Υ between 0.2 and 0.7, with the Kasteleyn transition at $\Upsilon = 1$. The most convincing agreement (Fig. 18) incorporates data points in the window $0.4 < B < 1.4$ T and $0.6 < T < 1.0$ K,

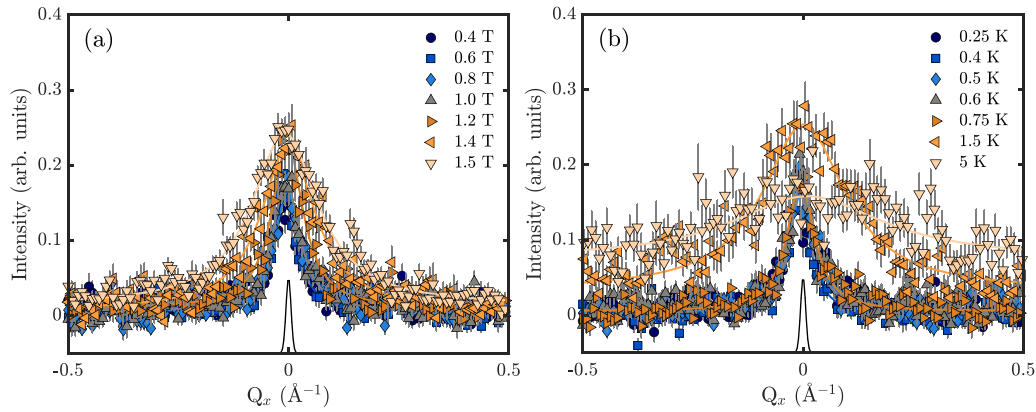


FIG. 17. Cuts through the experimental pinch point at $(0, \frac{2}{3})$ (a) as a function of field at a constant temperature of 0.75 K and (b) as a function of temperature at a constant field of 1 T. At constant temperature ($\Upsilon_K \propto B$) the pinch point broadening with field indicates a crossover out of the kagome ice phase. At constant field ($\Upsilon_K^{-1} \propto T$), the increase in background at 1.5 K suggests an increase in monopole population and a more paramagnetic state. At low temperature the pinch point width does not seem to decrease below $T \approx 0.6$ K.

with values of $\theta \approx 0.7^\circ$ and $\phi \approx 0^\circ$. We see that if the temperature is too low, the drift of the diffuse scattering features ceases; one plausible explanation is that the dynamics starts to slow down, as commonly observed in spin ice at this temperature [55]. Also, if the field is too large or too small or the temperature too high, the data depart from the scaling form as the kagome ice phase is no longer well defined. These two effects account for points at small or large Υ that depart from the scaling form.

V. DISCUSSION

In the following, we discuss our analytical, numerical, and experimental results together. We start in the kagome ice

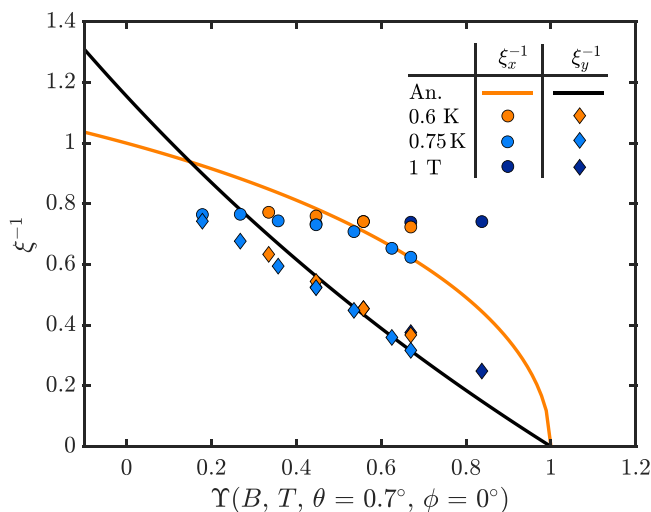


FIG. 18. Comparison between the analytical equation (8) (“An.”) and experimental correlation lengths as derived from the peak positions in the neutron scattering data, either at constant field or at constant temperature. The angle θ is chosen to be 0.7° as this best scales the data, while ϕ is chosen to be 0° , as suggested by the symmetry of the diffuse scattering maps.

phase far from a Kasteleyn transition and follow the evolution of the system towards the transition.

A. Critical correlations

1. Nontilted case

Although it proved difficult to approach the zero tilt condition exactly, both the in-kagome-plane spin correlations and the out-of-plane spin correlations that map to pseudospin degrees of freedom (see Fig. 14) have been observed and characterized. Our experimental measurements broadly confirm that $\text{Ho}_2\text{Ti}_2\text{O}_7$ gives an accurate realization of the two-dimensional nearest-neighbor kagome ice Coulomb phase, in the region of the phase diagram that is far from the experimentally observed critical end point at high field [15,22,56] or possible dipole driven ordering at low field [33,57]. Monopoles can be safely neglected in this regime, except insofar as they act as dynamical facilitators in the real system [58–60].

2. Tilted case

Our simulations and experiments clearly confirm that the applied tilted field can be used to quantitatively tune the Coulomb phase from isotropic to anisotropic. We have determined correlation lengths parallel and perpendicular to the applied field that scale differently as one moves towards the Kasteleyn transition, with a resulting buildup of anisotropic spin correlations.

When the methodology developed for the simulations is applied to the experimental data, we see that for moderate values of $\frac{\Upsilon}{\Upsilon_K}$, the analytical prediction captures the scaling of the correlation lengths extracted from the experimental data (Fig. 18). This illustrates that these qualitative features survive the corrections to the simple model that are necessary for a quantitative description of real materials: dipolar interactions, demagnetizing effects, and ice-rule-violating monopole excitations. We can firmly conclude that the framework of drifting peak positions encoding anisotropic scaling as the system is driven toward the Kasteleyn transition is relevant to a real material such as $\text{Ho}_2\text{Ti}_2\text{O}_7$.

3. Topological phase transition

Our thermodynamic results have illustrated several unusual features of the Kasteleyn transition: how it has no fluctuations below the transition and no symmetry breaking and yet satisfies all the thermodynamic and scaling criteria of a second-order phase transition. It is associated with a single thermodynamic variable and a single independent critical exponent. A crossover exponent to the paramagnetic phase can also be introduced by allowing a finite concentration of magnetic monopoles and forcing the monopole concentration to zero at the critical field [34].

Other examples of single-exponent transitions are the athermal percolation transition and the Kosterlitz-Thouless (KT) transition [61]. Other hard particle transitions, such as the crystallization of disks or spheres [44], or certain liquid-crystal transitions [45], although also purely entropic, do break symmetries and so generate a second thermodynamic variable related to the symmetry breaking.

There is a strong analogy between the Kasteleyn and the Kosterlitz-Thouless transition. Both are topological in that they involve the deconfinement of topological defects in an emergent electrostatic or magnetostatic field and both fail to break a symmetry. Applying the field introduces tension to the strings of coupled spins along the field direction and it is exactly this that gives the anisotropic scaling between the x and y directions: The strings are ballistic along the y axis but diffusive in the $d - 1$ dimensions perpendicular to the field. Despite the tension, the strings propagate above the transition because the entropy gain outweighs the string tension cost. In this sense the Kasteleyn transition can be thought of as a confinement-deconfinement transition for the magnetic monopole charges in very close analogy with the KT transition. Crucial differences are that, due to the field-induced anisotropy, the Kasteleyn transition exists in dimension greater than 2 and it produces real thermodynamic singularities, but it only survives in the limit of zero monopole concentration.

The string excitations are topological in that they change the topological sector of the emergent field [42,62] and are responsible for changing the magnetic moment of the sample, which distinguishes the Coulomb phase from a paramagnet [63]. In the critical region, the density of strings flipped against the ordered moment falls to zero, so they can be considered as weakly interacting, mapping onto world lines for individual random walkers. In this limit, the in-plane field direction dictates the commensurability of the string looping on the torus. We have identified a crossover, with in-plane tilt ϕ , to an incommensurate limit in which individual strings influence the total moment [43]. This remarkable topological property of the finite-size-scaling features strictly depends on the existence of a torus and so may be hard to realize in a real system, where extended strings must terminate in surface magnetic charge [64] or defects [65].

4. Kasteleyn transition in experiment

While our numerical simulations can be driven right to a Kasteleyn transition, the experimental system could not be, being complicated by the slowing down of collective dy-

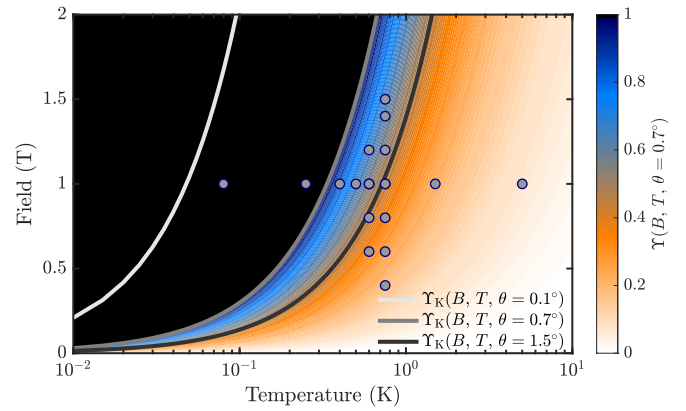


FIG. 19. Field and temperatures that satisfy the Kasteleyn transition criterion at $\theta = 0.1^\circ$, 0.7° , and 1.5° , with the experimentally measured data points shown by circles. The solid lines show the loci of $\Upsilon_K = 1$ for three different field tilts; the color map shows Υ_K for $\theta = 0.7$. With the θ and ϕ derived from the crystal alignment by Laue diffraction, no point in the phase space is above the critical point for the Kasteleyn phase transition ($\Upsilon_K = 1$). For the values that best scale the data (i.e., $\theta = 0.7^\circ$), only points within the regime of slow dynamics fall below the transition. To move the transition into a region where we could comfortably measure, the larger tilt of $\theta = 1.5^\circ$ would be required.

namics below $T \approx 0.6$ K and the onset (termination) of the kagome plateau at $H \approx 0.4$ (1.5) T. Within the kagome ice plateau, for fixed tilt, as in a typical experiment, to reach larger Υ requires larger fields or lower temperatures. Increasing the field too much will proliferate monopoles and terminate the kagome ice plateau, but lowering the temperature will tend to cause $\text{Ho}_2\text{Ti}_2\text{O}_7$ to run out of dynamics as the monopoles disappear. Figure 19 summarizes the field and temperature points accessed in our experiments and compares the Kasteleyn criterion for our estimated tilt, along with a smaller and larger value. This suggests that the tilt required to access the transition would be experimentally accessible, but in this case the transition is likely to be rounded by the eventual monopole contribution, as was shown for the three-dimensional example [30,66]. However, the incorporation of monopoles can also lead to unconventional behavior and scaling [34,67]. Sharper transitions at lower temperature that could be obtained with a smaller tilt would be unobservable as they would fall deep in the frozen regime. Approaching closer to the transition, one also expects small corrections to the above scaling form due to the presence of dipole interactions and subsequent corrections to the monopole picture, as has been shown in three dimensions [33].

However, rather than promoting the transition in classical spin ices such as $\text{Ho}_2\text{Ti}_2\text{O}_7$ and $\text{Dy}_2\text{Ti}_2\text{O}_7$ into regions of phase space where other phenomena are crowded, perhaps it can be reached by studying a compound with faster monopole dynamics such as CdEr_2S_4 [68]. In this case, the spin ice is classical and the thermal monopole population is fairly similar to $\text{Dy}_2\text{Ti}_2\text{O}_7$, but hopping rates are much more rapid, suggesting that equilibrium can be maintained to lower temperature. An alternative source of dynamics might be quantum fluctuations, and a quantum kagome ice phase could be a highly

interesting system, as realized in a magnetization plateau of a quantum spin ice [69–71] or a two-dimensional kagome analog of spin ice [72]. We are not aware of any theoretical study of the Kasteleyn transition in a quantum kagome ice [73,74], which might also be a fascinating prospect, given the interest in quantum spin ice [69,75,76].

VI. CONCLUSION

We have studied the Kasteleyn transition in the kagome ice phase of spin ice subjected to a field tilted away from the [111] direction by a small angle, by analytical, numerical, and experimental methods. We have exposed a striking evolution of correlations and of topological properties of the Coulomb phase as the field is tuned towards the transition.

We found good qualitative agreement between experimental neutron scattering results from a single crystal of $\text{Ho}_2\text{Ti}_2\text{O}_7$ and those provided by the nearest-neighbor spin ice model. The agreement is perhaps better than in the three-dimensional zero-field regime of spin ice, where inclusion of the full dipolar interaction is essential to reproduce the broad features of the diffuse scattering [20,77–81] and it would be interesting to investigate this point further. Consequently, we may be very optimistic that yet more of the exotic behavior of kagome ice will be experimentally observable in spin ice materials.

ACKNOWLEDGMENTS

We thank Ch. Ruëgg for comments on this work and Ref. [82] and L. Jaubert and T. Roscilde for useful discussions. Neutron scattering experiments were carried out on D7 at the ILL, Grenoble, France. Work at PSI was partly funded by the Schweizerischer Nationalfonds zur Förderung der Wissenschaftlichen Forschung Grants No. 200021_140862 and No. 200020_162626). P.C.W.H. acknowledges financial support from ANR, France, Grant No. ANR-19-CE30-0040. I.G.W. acknowledges financial support from NERC Grant No. GR3/7497.

APPENDIX A: RELATION WITH KAGOME SPIN ICE

Prior to the discovery of kagome ice, Wills *et al.* [83] introduced a two-dimensional version of spin ice consisting of ferromagnetically coupled Ising-like spins on a kagome lattice, constrained to point in or out of the triangles. This state, which they called kagome spin ice, is a very interesting system its own right and has a rich phase diagram when long-range interactions are included [35,36,84]. It is highly relevant to artificial spin ice arrays and has been much studied in this context [85]. Here we reserve the term kagome ice for the state obtained when the magnetic field is applied in the [111] direction of a spin ice and the term kagome spin ice for the model of Wills *et al.* We identify similarities and differences between the two systems and to highlight the topological constraints of the kagome ice state [4].

In kagome spin ice the lowest-energy configuration on each triangle satisfies an icelike rule with either two in and one out or one in and two out. The odd number of in/out contributions leaves a net charge of $\pm Q/2$ associated with each triangle, where Q is the monopole charge. The ground

state of the nearest-neighbor model is therefore a dense charge fluid with overall charge neutrality [86], the so-called KI phase. Including long-range dipolar interactions induces a phase transition at finite temperature from the fully disordered KI phase to the partially ordered KII phase [35,36], even in the absence of ice-rule defects [87]. The transition is driven by a Z_2 symmetry breaking in which up- and down-oriented triangles select between two-in–one-out or one-in–two-out configurations, lifting a topological degeneracy that allows for the formation of system spanning spin loops [4]. The reduced symmetry corresponds to charge crystallization [35,36,84] but only partial magnetic ordering [32]. For perfect charge order, the spins effectively decouple, or fragment, into two independent parts, longitudinal and transverse, with the transverse part forming a Coulomb phase with corresponding algebraic correlations. In dipolar kagome spin ice, corrections to the emergent Coulomb interaction between monopoles lead to a further transition at low temperature, to a fully ordered phase in analogy with dipolar spin ice [88].

The application of the field along [111] in a spin ice breaks this Z_2 symmetry for the spins on the kagome plane by pinning the apical spin of each tetrahedron (discussed below). Applying the ice rules with this constraint imposes the reduced choice of two in and one out or one in and two out for the three remaining spins.

The kagome ice phase therefore corresponds to the KII phase of dipolar kagome spin ice. In this case, the remnant charge of the three in-plane spins is neutralized by the charge on the apical spin giving charge neutrality. In this limit the spin ice Coulomb phase is split into decoupled planes, each of which has the configuration space of the KII phase.

APPENDIX B: KASTELEYN TRANSITION TEMPERATURE

As described above, a kagome ice spin configuration with long-range order is disordered at the Kasteleyn transition through the introduction of strings of reversed spins spanning the entire cell and passing through the periodic boundaries. Here we present some details for this process for general tilt θ and ϕ .

We start with the magnetically ordered state shown in Fig. 20, defined with all vertices in configuration 1. This ordering is along along the $[\bar{1}\bar{1}2]$ or y crystal axis, as defined for the underlying pyrochlore lattice (see also Figs. 1 and 2). There is an in-plane field \vec{H} , placed at an angle ϕ with respect to y . The probability of introducing a string goes to zero at the Kasteleyn transition temperature T_K , which can be calculated by estimating the free-energy change $\delta G = \delta\langle\mathcal{H}\rangle - T\delta S$ on introducing the string. Here $\delta\langle\mathcal{H}\rangle$ is the change in magnetic enthalpy, which in our constrained model is pure Zeeman

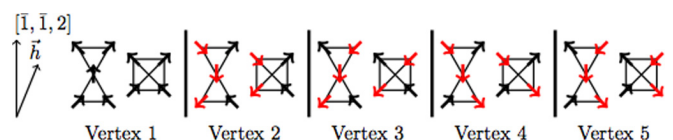


FIG. 20. The five vertices relevant to the Kasteleyn transition on the kagome lattice.

energy and δS is the change in entropy. The unit cell is taken to be an up triangle of the kagome lattice. For a system spanning L cells in the y direction, we can define $\delta G = L\delta g$, $\delta\langle\mathcal{H}\rangle = L\delta\epsilon$, and $\delta S = L\delta s$. We are therefore looking for a change in sign in $\delta g = \delta\epsilon - T\delta s$: $\delta\epsilon = T_K\delta s$.

At each step of the string construction, the virtual head of the string, or worm, can be thought of as sitting in the center of a down triangle. It advances by jumping from this site through an up triangle to a neighboring down triangle. The Zeeman energy to be considered is the change in energy coming from flipping the two spins on the up triangle through which the worm hops. Considering the five-spin up-down triangle pair in Fig. 20, we calculate the probabilities that vertex 1 changes to vertices 2–5. The worm head arrives in the down triangle at the end of the $(n-1)$ th step, and the probability of it arriving from left or right is taken care of during this step. As this is a Markov process, the n th step is independent of this, and in this step it jumps down and out of view to the left or right. Consequently, the Boltzmann weights for the five vertices are proportional to the dimer fugacities defined following Eq. (2), i.e., $w_1 \propto z_1$, $w_2 = w_3 \propto z_2$, and $w_4 = w_5 \propto z_3$, and there are only two probabilities for an evolution from vertex 1: $P_L = P_{1\rightarrow 2} = P_{1\rightarrow 3}$ and $P_R = P_{1\rightarrow 4} = P_{1\rightarrow 5}$.

The changes in Zeeman energy associated with this move are

$$\begin{aligned}\epsilon_L &= 2HS_\perp \cos(\phi) + 2HS_\perp \cos(\pi/3 - \phi) \\ &= 3HS_\perp \cos(\phi) + \sqrt{3}HS_\perp \sin(\phi),\end{aligned}\quad (\text{B1})$$

$$\epsilon_R = 3HS_\perp \cos(\phi) - \sqrt{3}HS_\perp \sin(\phi).\quad (\text{B2})$$

Given that $S_\perp = 2\sqrt{2}/3$, we have

$$\epsilon_{L,R} = \epsilon_0 \pm v,\quad (\text{B3})$$

where $\epsilon_0 = 2\sqrt{2}H \cos(\phi)$ and $v = 2\sqrt{\frac{2}{3}}H \sin(\phi)$.

The probabilities are then given by

$$P_{L,R} = \frac{\exp(\mp\beta v)}{\exp(\beta v) + \exp(-\beta v)},\quad (\text{B4})$$

where $P_L + P_R = 1$ and $P_L/P_R = \exp[-\beta(\epsilon_L - \epsilon_R)] = \exp(-2\beta v)$. Defining $P_{L,R} = \frac{1}{2}(1 \mp q)$, we find $q = \tanh(\beta v)$. From this we can write $\delta\epsilon = P_L\epsilon_L + P_R\epsilon_R = \epsilon_0 + v(P_L - P_R) = \epsilon_0 - qv$ and

$$\begin{aligned}\frac{1}{k_B}\delta s &= -P_L \log P_L - P_R \log P_R \\ &= -\left(\frac{1-q}{2}\right) \log\left(\frac{1-q}{2}\right) \\ &\quad -\left(\frac{1+q}{2}\right) \log\left(\frac{1+q}{2}\right).\end{aligned}\quad (\text{B5})$$

We can now use the identities

$$\frac{1}{4}(1+q)(1-q) = \frac{1}{4\cosh^2(\beta v)},\quad (\text{B6})$$

$$\frac{1+q}{1-q} = \exp(2\beta v),\quad (\text{B7})$$

$$\beta qv = \frac{q}{2} \log(\exp 2\beta v)\quad (\text{B8})$$

to show that, for $T = T_K$,

$$\frac{\epsilon_0}{k_B T} = \log[2 \cosh(\beta v)].\quad (\text{B9})$$

Exponentiating both sides, changing units, and using Eq. (3), we arrive at Eq. (4).

APPENDIX C: LOOP ALGORITHM FOR KAGOME ICE

The loop algorithm for numerical simulations is constructed in this spirit. Creating a worm requires the creation of a pair of oppositely charged topological defects which are considered as virtual, in that the Boltzmann weight for their creation is never taken into account. The worm makes a path of virtual hops which can be either forward, backward, or sideways until it returns to its starting position, destroying the defect pair and recovering their creation energy. A set of transition probabilities can be found by identifying $P_{1\rightarrow 2} = P_L$ and $P_{1\rightarrow 4} = P_R$. The reverse probabilities $P_{2\rightarrow 1}$ and $P_{4\rightarrow 1}$ satisfy detailed balance: $P_{2\rightarrow 1} = P_L(\frac{z_1}{z_2})$ and $P_{4\rightarrow 1} = P_R(\frac{z_1}{z_3})$. As for general ϕ , $\mu_1 - \mu_2 = \epsilon_0 + v$ and

$$P_{2\rightarrow 1} = \exp\{\beta\epsilon_0 - \log[2 \cosh(\beta v)]\}\quad (\text{C1})$$

so that $P_{2\rightarrow 1} \rightarrow 1$ at T_K , which is the condition one needs for singular behavior at the Kasteleyn transition. For the case $z_3 > z_2$ we can set $P_{2\rightarrow 4} = 1 - P_{2\rightarrow 1}$ so that $P_{2\rightarrow 4} \rightarrow 0$ at T_K . The right to left transition is fixed by detailed balance $P_{4\rightarrow 2} = P_{2\rightarrow 4}(\frac{z_2}{z_3})$. Following this, the satisfaction of global balance for flow out of vertex 4 requires the introduction of a backtracking probability $P_{4\rightarrow 4}$ proportional to $z_3 - z_2$. However, this set of probabilities is not unique and other sets exist which avoid backtracking.

APPENDIX D: DIMER REPRESENTATION OF THE KASTELEYN TRANSITION FOR GENERAL ϕ

The dimer partition function can be written

$$Z = \text{Tr}_{\{n_1, n_2, n_3\}} g(n_1, n_2, n_3) \exp[\beta(n_1\mu_1 + n_2\mu_2 + n_3\mu_3)],\quad (\text{D1})$$

where n_i is the number of dimers on sites i and $g(n_1, n_2, n_3)$ is the number of configurations for fixed n_i . The total number of dimers n is fixed at one per triangle, so we can define a semigrand canonical free energy [89] (also the magnetic free energy) $G(T, n, \mu_1, \mu_2, \mu_3)$. The Z can be calculated exactly by the Pfaffian method introduced by Kasteleyn [27]. Although Kasteleyn does not give an explicit expression for the honeycomb lattice, Wu [90] does, while at the same time showing how the dimers on the honeycomb and therefore spins on the kagome lattice also map onto the five-vertex model on a square lattice. The anisotropic six-vertex model was also treated exactly by Watson [91]. Wu's expression for Z is

$$\begin{aligned}\log Z &= \frac{n}{8\pi^2} \int_0^{2\pi} d\tilde{\theta} \int_0^{2\pi} d\tilde{\phi} \log [z_1^2 + z_2^2 + z_3^2 \\ &\quad + 2z_1z_2 \cos(\tilde{\theta}) + 2z_1z_3 \cos(\tilde{\phi}) + 2z_2z_3 \cos(\tilde{\theta} - \tilde{\phi})],\end{aligned}\quad (\text{D2})$$

where $\tilde{\theta}$ and $\tilde{\phi}$ are dummy variables.

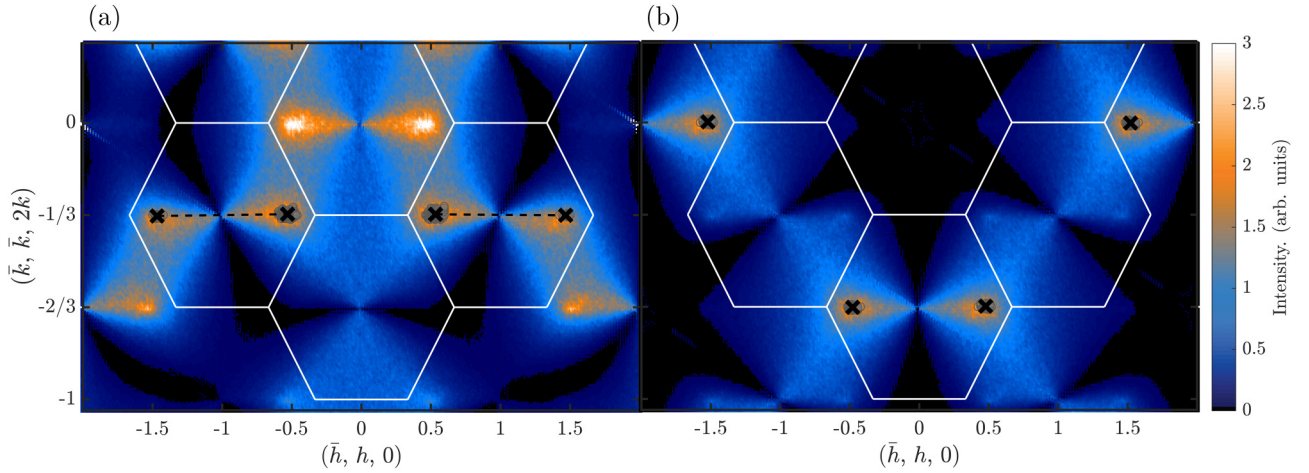


FIG. 21. Results of the peak tracking algorithm in (a) the spin-flip and (b) the non-spin-flip channel for $\Upsilon = 0.54$ (i.e., 1 T, 0.75 K, $\theta > 0$, and $\phi = 0$), with included data points in gray dots. The centers of the asymmetrical ellipses as determined by the fuzzy cluster algorithm are marked with a black \times and correspond to the actual location of the calculated local maxima, and the distance between the peaks used to compute ξ_x is shown by a black dashed line in the SF channel. The mean membership grade for this peak tracking solution is $\mu^m = 0.98$.

From the above one can calculate the mean number of dimers

$$\langle n_{2,3} \rangle = -\frac{\partial G}{\partial \mu_{2,3}} = \frac{1}{\beta} \frac{\partial \log Z}{\partial \mu_{2,3}}. \quad (\text{D3})$$

As the total number of dimers is fixed, $\langle n_1 \rangle$ is not independent: $\langle n_1 \rangle = n - \langle n_2 \rangle - \langle n_3 \rangle$. Defining $\alpha_i = \langle n_i \rangle / n$, one finds from the exact partition function

$$\begin{aligned} \alpha_2 &= \frac{1}{\pi} \cos^{-1} \left(\frac{z_3^2 - z_2^2 + z_1^2}{2z_1 z_3} \right), \\ \alpha_3 &= \frac{1}{\pi} \cos^{-1} \left(\frac{z_2^2 - z_3^2 + z_1^2}{2z_1 z_2} \right), \end{aligned} \quad (\text{D4})$$

with $\alpha_1 = 1 - \alpha_2 - \alpha_3$. To arrive at this expression, one needs the identity

$$\int_0^{2\pi} d\theta \frac{1}{A + B \cos(\theta) + C \sin(\theta)} = \frac{2\pi}{(A^2 - B^2 - C^2)^{1/2}}, \quad (\text{D5})$$

which is valid for $A^2 > B^2 + C^2$, corresponding to the disordered regime $z_2 + z_3 > z_1$. At high temperature $\langle n_1 \rangle = \langle n_2 \rangle = \langle n_3 \rangle = n/3$, while at the transition $\langle n_1 \rangle = 1$, $\langle n_2 \rangle = \langle n_3 \rangle = 0$. As the thermodynamic variable reaches the constraint, no further evolution can occur and the system is singular. It follows straightforwardly that the mean energy per spin, which is $\frac{1}{3}$ of the mean energy per dimer, is

$$\begin{aligned} \langle \epsilon \rangle &= -\frac{1}{3n} (\mu_1 n_1 + \mu_2 n_2 + \mu_3 n_3) \\ &= -\frac{1}{3} [\mu_1 + \alpha_2 (\mu_2 - \mu_1) + \alpha_3 (\mu_3 - \mu_1)]. \end{aligned} \quad (\text{D6})$$

The in-plane magnetization can also be calculated from the mean dimer numbers by considering each of the three spins separately: $\langle S_1^y \rangle = S_\perp$ when $\langle n_1 \rangle = 1$ and $\langle S_1^y \rangle = -S_\perp/3$ when $\langle n_1 \rangle = \frac{1}{3}$, from which it follows that $\langle S_1^y \rangle = S_\perp(2\alpha_1 - 1)$. Similarly $\langle S_2^y \rangle = 1/2 S_\perp$ when $\langle n_2 \rangle = 0$ and $\langle S_2^y \rangle = S_\perp/6$ when $\langle n_2 \rangle = \frac{1}{3}$, from which we find $\langle S_2^y \rangle = S_\perp(-\alpha_2 + \frac{1}{2})$,

with the equivalent expression for the third spin, $\langle S_3^y \rangle = S_\perp(-\alpha_3 + \frac{1}{2})$. The total y component of the magnetization (per spin, hence the factor $\frac{1}{3}$) is then $M_y = (S_\perp/3)(2\alpha_1 - \alpha_2 - \alpha_3)$.

For the x component, $\langle S_1^x \rangle = 0$, $\langle S_2^x \rangle = (\sqrt{3}/2)S_\perp$ when $\langle n_2 \rangle = 0$ and $\langle S_2^x \rangle = \frac{1}{3}(\sqrt{3}/2)S_\perp$ when $\langle n_2 \rangle = \frac{1}{3}$, leading to $\langle S_2^x \rangle = \sqrt{3}S_\perp(-\alpha_2 + \frac{1}{2})$ and to $\langle S_3^x \rangle = \sqrt{3}S_\perp(\alpha_3 - \frac{1}{2})$. This gives the average x component per spin, $M_x = \frac{1}{3}\sqrt{3}S_\perp(\alpha_3 - \alpha_2)$. Using the relation between the α_i and the value $S_\perp = 2\sqrt{2}/3$, we finally find the correct expressions for M_y and M_x parallel and perpendicular to $[\bar{1}\bar{1}2]$:

$$\begin{aligned} M_y &= \frac{4\sqrt{2}}{9} \left(1 - \frac{3}{2}(\alpha_2 + \alpha_3) \right), \\ M_x &= \frac{2}{3} \sqrt{\frac{2}{3}} (\alpha_3 - \alpha_2). \end{aligned} \quad (\text{D7})$$

The dimensionless magnetic moment entering the thermodynamic discussion above would correspond to $M = NM_y$.

APPENDIX E: PEAK TRACKING ALGORITHM

From tracking the logarithmic peak locations in the diffuse neutron scattering patterns and determining their distance from the Brillouin zone center, we can reproduce the normalized inverse correlations ξ_x^{-1} and ξ_y^{-1} [3]. The location of diffuse scattering peaks close to $h = -\frac{1}{2}$ and $-\frac{3}{2}$ and $k = \pm\frac{1}{3}$ were extracted with a two-dimensional peak tracking program based on the fuzzy cluster algorithm in MATLAB, in which an initial guess for the location of four diffuse scattering peaks is refined by measuring the membership grades μ_{ij} of each point in reciprocal space with intensities higher than 5 times the background threshold [92]. To get the cluster centers c , the following objective function J_m for D data points and $N = 4$

clusters is minimized:

$$J_m = \sum_{i=1}^D \sum_{j=1}^N \mu_{ij}^m |x_i - c_j|^2. \quad (\text{E1})$$

The membership grades of each point in the cluster demonstrates the relative uncertainty that the point is indeed in that cluster, with values approaching 1 for a collection of distinct spherical clusters. Although not as sharp as Bragg peaks, the logarithmic peaks indicative of short-range ice-rule correlations are clearly distinguishable in both simulation and experimental data from the background with

clear centers. Peaks from an experimental diffuse scattering patterns with an unknown misalignment can therefore be analyzed generically.

The distance from each diffuse peak to the kagome Brillouin zone center (as denoted by the white hexagons in Fig. 21) along $(\bar{h}, h, 0)$ was averaged to produce the inverse correlation length ξ_x^{-1} , from which the analytical solution in Eq. (8) was used to derive ξ_y^{-1} . As the nearest-neighbor Hamiltonian produces logarithmic peaks that have a small tail along $(\bar{h}, h, 0)$, there is a slight deviation of the cluster center from the true maximum, which is less than 0.01 \AA^{-1} for all simulations.

-
- [1] M. J. Harris, S. T. Bramwell, T. Zeiske, D. F. McMorrow, and P. J. C. King, Magnetic structures of highly frustrated pyrochlores, *J. Magnetism Magnetic Materials* **177–181**, 757 (1998).
- [2] K. Matsuhira, Z. Hiroi, T. Tayama, S. Takagi, and T. Sakakibara, A new macroscopically degenerate ground state in the spin ice compound $\text{Dy}_2\text{Ti}_2\text{O}_7$ under a magnetic field, *J. Phys.: Condens. Matter* **14**, L559 (2002).
- [3] R. Moessner and S. L. Sondhi, Theory of the [111] magnetization plateau in spin ice, *Phys. Rev. B* **68**, 064411 (2003).
- [4] A. J. Macdonald, P. C. W. Holdsworth, and R. G. Melko, Classical topological order in kagome ice, *J. Phys.: Condens. Matter* **23**, 164208 (2011).
- [5] J. F. Nagle, Lipid bilayer phase transition: Density measurements and theory, *Proc. Natl. Acad. Sci. U.S.A.* **70**, 3443 (1973).
- [6] F. Alet, G. Misguich, V. Pasquier, R. Moessner, and J. L. Jacobsen, Unconventional Continuous Phase Transition in a Three-Dimensional Dimer Model, *Phys. Rev. Lett.* **97**, 030403 (2006).
- [7] S. Powell, Higgs transitions of spin ice, *Phys. Rev. B* **84**, 094437 (2011).
- [8] R. J. Baxter, *Exactly Solved Models in Statistical Mechanics* (Academic, London, 1982).
- [9] T. Sakakibara, T. Tayama, Z. Hiroi, K. Matsuhira, and S. Takagi, Observation of a Liquid-Gas-Type Transition in the Pyrochlore Spin Ice Compound $\text{Dy}_2\text{Ti}_2\text{O}_7$ in a Magnetic Field, *Phys. Rev. Lett.* **90**, 207205 (2003).
- [10] H. Fukazawa, R. G. Melko, R. Higashinaka, Y. Maeno, and M. J. P. Gingras, Magnetic anisotropy of the spin-ice compound $\text{Dy}_2\text{Ti}_2\text{O}_7$, *Phys. Rev. B* **65**, 054410 (2002).
- [11] Z. Hiroi, K. Matsuhira, T. Tayama, S. Takagi, and T. Sakakibara, Specific heat of kagome ice in the pyrochlore oxide $\text{Dy}_2\text{Ti}_2\text{O}_7$, *J. Phys. Soc. Jpn.* **72**, 411 (2003).
- [12] H. Aoki, T. Sakakibara, K. Matsuhira, and Z. Hiroi, Magnetocaloric effect study on the pyrochlore spin ice compound $\text{Dy}_2\text{Ti}_2\text{O}_7$ in a [111] magnetic field, *J. Phys. Soc. Jpn.* **73**, 2851 (2004).
- [13] Y. Tabata, H. Kadowaki, K. Matsuhira, Z. Hiroi, N. Aso, E. Ressouche, and B. Fåk, Kagomé Ice State in the Dipolar Spin Ice $\text{Dy}_2\text{Ti}_2\text{O}_7$, *Phys. Rev. Lett.* **97**, 257205 (2006).
- [14] T. Fennell, S. T. Bramwell, D. F. McMorrow, P. Manuel, and A. R. Wildes, Pinch points and Kasteleyn transitions in kagome ice, *Nat. Phys.* **3**, 566 (2007).
- [15] H. Kadowaki, N. Doi, Y. Aoki, Y. Tabata, T. J. Sato, J. W. Lynn, K. Matsuhira, and Z. Hiroi, Observation of Magnetic Monopoles in Spin Ice, *J. Phys. Soc. Jpn.* **78**, 103706 (2009).
- [16] J. D. Bernal and R. H. Fowler, A theory of water and ionic solution, with particular reference to hydrogen and hydroxyl ions, *J. Chem. Phys.* **1**, 515 (1933).
- [17] L. Pauling, The structure and entropy of ice and of other crystals with some randomness of atomic arrangement, *J. Am. Chem. Soc.* **57**, 2680 (1935).
- [18] S. T. Bramwell and M. J. Harris, Frustration in Ising-type spin models on the pyrochlore lattice, *J. Phys.: Condens. Matter* **10**, L215 (1998).
- [19] C. L. Henley, The “Coulomb phase” in frustrated systems, *Annu. Rev. Condens. Matter Phys.* **1**, 179 (2010).
- [20] T. Fennell, P. P. Deen, A. R. Wildes, K. Schmalzl, D. Prabhakaran, A. T. Boothroyd, R. J. Aldus, D. F. McMorrow, and S. T. Bramwell, Magnetic Coulomb phase in the spin ice $\text{Ho}_2\text{Ti}_2\text{O}_7$, *Science* **326**, 415 (2009).
- [21] C. Krey, S. Legl, S. R. Dunsiger, M. Meven, J. S. Gardner, J. M. Roper, and C. Pfleiderer, First Order Metamagnetic Transition in $\text{Ho}_2\text{Ti}_2\text{O}_7$ Observed by Vibrating Coil Magnetometry at Milli-Kelvin Temperatures, *Phys. Rev. Lett.* **108**, 257204 (2012).
- [22] C. Castelnovo, R. Moessner, and S. L. Sondhi, Magnetic monopoles in spin ice, *Nature (London)* **451**, 42 (2008).
- [23] V. Raban, C. T. Suen, L. Berthier, and P. C. W. Holdsworth, Multiple symmetry sustaining phase transitions in spin ice, *Phys. Rev. B* **99**, 224425 (2019).
- [24] D. A. Huse, W. Krauth, R. Moessner, and S. L. Sondhi, Coulomb and Liquid Dimer Models in Three Dimensions, *Phys. Rev. Lett.* **91**, 167004 (2003).
- [25] S. Powell and J. T. Chalker, Classical to quantum mappings for geometrically frustrated systems: Spin-ice in a [100] field, *Phys. Rev. B* **78**, 024422 (2008).
- [26] S. Powell and J. T. Chalker, $\text{SU}(2)$ -Invariant Continuum Theory for an Unconventional Phase Transition in a Three-Dimensional Classical Dimer Model, *Phys. Rev. Lett.* **101**, 155702 (2008).
- [27] P. W. Kasteleyn, Dimer statistics and phase transitions, *J. Math. Phys.* **4**, 287 (1963).
- [28] A. M. Läuchli, S. Capponi, and F. F. Assaad, Dynamical dimer correlations at bipartite and non-bipartite Rokhsar-Kivelson points, *J. Stat. Mech.* (2008) P01010.

- [29] W. H. Kao, P. C. W. Holdsworth, and Y. J. Kao, Field-induced ordering in dipolar spin ice, *Phys. Rev. B* **93**, 180410(R) (2016).
- [30] L. D. C. Jaubert, J. T. Chalker, P. C. W. Holdsworth, and R. Moessner, Three-Dimensional Kasteleyn Transition: Spin Ice in a [100] Field, *Phys. Rev. Lett.* **100**, 067207 (2008).
- [31] L. D. C. Jaubert and P. C. W. Holdsworth, Signature of magnetic monopole and Dirac string dynamics in spin ice, *Nat. Phys.* **5**, 258 (2009).
- [32] M. E. Brooks-Bartlett, S. T. Banks, L. D. C. Jaubert, A. Harman-Clarke, and P. C. W. Holdsworth, Magnetic-Moment Fragmentation and Monopole Crystallization, *Phys. Rev. X* **4**, 011007 (2014).
- [33] M. L. Baez and R. A. Borzi, The 3D Kasteleyn transition in dipolar spin ice: A numerical study with the conserved monopoles algorithm, *J. Phys.: Condens. Matter* **29**, 055806 (2017).
- [34] S. Powell, Confinement of monopoles and scaling theory near unconventional critical points, *Phys. Rev. B* **87**, 064414 (2013).
- [35] G. Möller and R. Moessner, Magnetic multipole analysis of kagome and artificial spin-ice dipolar arrays, *Phys. Rev. B* **80**, 140409(R) (2009).
- [36] G.-W. Chern, P. Mellado, and O. Tchernyshyov, Two-Stage Ordering of Spins in Dipolar Spin Ice on the Kagome Lattice, *Phys. Rev. Lett.* **106**, 207202 (2011).
- [37] P. W. Anderson, Ordering and antiferromagnetism in ferrites, *Phys. Rev.* **102**, 1008 (1956).
- [38] A. Harman-Clarke, Topological constraints and ordering in model frustrated magnets, Ph.D. thesis, University College London, 2010.
- [39] Z. Hiroi, K. Matsuhira, and M. Ogata, Ferromagnetic Ising spin chains emerging from the spin ice under magnetic field, *J. Phys. Soc. Jpn.* **72**, 3045 (2003).
- [40] T. Fennell, O. A. Petrenko, B. Fåk, J. S. Gardner, S. T. Bramwell, and B. Ouladdiaf, Neutron scattering studies of the spin ices $\text{Ho}_2\text{Ti}_2\text{O}_7$ and $\text{Dy}_2\text{Ti}_2\text{O}_7$ in applied magnetic field, *Phys. Rev. B* **72**, 224411 (2005).
- [41] J. P. C. Ruff, R. G. Melko, and M. J. P. Gingras, Finite-Temperature Transitions in Dipolar Spin Ice in a Large Magnetic Field, *Phys. Rev. Lett.* **95**, 097202 (2005).
- [42] L. D. C. Jaubert, M. J. Harris, T. Fennell, R. G. Melko, S. T. Bramwell, and P. C. W. Holdsworth, Topological-Sector Fluctuations and Curie-Law Crossover in Spin Ice, *Phys. Rev. X* **3**, 011014 (2013).
- [43] S. M. Bhattacharjee, J. F. Nagle, D. A. Huse, and M. E. Fisher, Critical behavior of a three-dimensional dimer model, *J. Stat. Phys.* **32**, 361 (1983).
- [44] B. J. Alder and T. E. Wainwright, Studies in molecular dynamics. II. Behavior of a small number of elastic spheres, *J. Chem. Phys.* **33**, 1439 (1960).
- [45] M. Dijkstra and D. Frenkel, Evidence for Entropy-Driven Demixing in Hard-Core Fluids, *Phys. Rev. Lett.* **72**, 298 (1994).
- [46] L. D. C. Jaubert, *Topological Constraints and Defects in Spin Ice* (ENS Lyon, Lyon, 2009).
- [47] N. Goldenfeld, *Renormalization Group in Critical Phenomena* (Addison-Wesley, Reading, 1994).
- [48] S. Powell, Ferromagnetic Coulomb phase in classical spin ice, *Phys. Rev. B* **91**, 094431 (2015).
- [49] J. R. Stewart, P. P. Deen, K. H. Andersen, H. Schober, J.-F. Barthélémy, J. M. Hillier, A. P. Murani, T. Hayes, and B. Lindenau, Disordered materials studied using neutron polarization analysis on the multi-detector spectrometer, D7, *J. Appl. Crystallogr.* **42**, 69 (2009).
- [50] H. T. Diep, *Frustrated Spin Systems*, 2nd ed. (World Scientific, Singapore, 2013).
- [51] D. J. P. Morris, D. A. Tennant, S. A. Grigera, B. Klemke, C. Castelnovo, R. Moessner, C. Czternasty, M. Meissner, K. C. Rule, J. U. Hoffman, K. Kiefer, S. Gerischer, D. Slobinsky, and R. S. Perry, Dirac strings and magnetic monopoles in the spin ice $\text{Dy}_2\text{Ti}_2\text{O}_7$, *Science* **326**, 411 (2009).
- [52] J. A. Quilliam, L. R. Yaraskavitch, H. A. Dabkowska, B. D. Gaulin, and J. B. Kycia, Dynamics of the magnetic susceptibility deep in the Coulomb phase of the dipolar spin ice material $\text{Ho}_2\text{Ti}_2\text{O}_7$, *Phys. Rev. B* **83**, 094424 (2011).
- [53] L. Bovo, L. D. C. Jaubert, P. C. W. Holdsworth, and S. T. Bramwell, Crystal shape-dependent magnetic susceptibility and Curie law crossover in the spin ices $\text{Dy}_2\text{Ti}_2\text{O}_7$ and $\text{Ho}_2\text{Ti}_2\text{O}_7$, *J. Phys.: Condens. Matter* **25**, 386002 (2013).
- [54] M. Twengström, L. Bovo, M. J. P. Gingras, S. T. Bramwell, and P. Henelius, Microscopic aspects of magnetic lattice demagnetizing factors, *Phys. Rev. Materials* **1**, 044406 (2017).
- [55] C. Paulsen, M. J. Jackson, E. Lhotel, B. Canals, D. Prabhakaran, K. Matsuhira, S. R. Giblin, and S. T. Bramwell, Far-from-equilibrium monopole dynamics in spin ice, *Nat. Phys.* **10**, 135 (2014).
- [56] R. A. Borzi, F. A. Gómez Albarracín, H. D. Rosales, G. L. Rossini, A. Steppke, D. Prabhakaran, A. P. Mackenzie, D. C. Cabra, and S. A. Grigera, Intermediate magnetisation state and competing orders in $\text{Dy}_2\text{Ti}_2\text{O}_7$ and $\text{Ho}_2\text{Ti}_2\text{O}_7$, *Nat. Commun.* **7**, 12592 (2016).
- [57] R. G. Melko, B. C. den Hertog, and M. J. P. Gingras, Long-Range Order at Low Temperatures in Dipolar Spin Ice, *Phys. Rev. Lett.* **87**, 067203 (2001).
- [58] H. Takatsu, K. Goto, H. Otsuka, R. Higashinaka, K. Matsubayashi, Y. Uwatoko, and H. Kadowaki, Two-dimensional monopole dynamics in the dipolar spin ice $\text{Dy}_2\text{Ti}_2\text{O}_7$, *J. Phys. Soc. Jpn.* **82**, 073707 (2013).
- [59] H. Otsuka, H. Takatsu, K. Goto, and H. Kadowaki, Scaling ansatz for the ac magnetic response in two-dimensional spin ice, *Phys. Rev. B* **90**, 144428 (2014).
- [60] R. A. Borzi, D. Slobinsky, and S. A. Grigera, Charge Ordering in a Pure Spin Model: Dipolar Spin Ice, *Phys. Rev. Lett.* **111**, 147204 (2013).
- [61] J. M. Kosterlitz and D. J. Thouless, Ordering, metastability and phase transitions in two-dimensional systems, *J. Phys. C* **6**, 1181 (1973).
- [62] M. F. Faulkner, S. T. Bramwell, and P. C. W. Holdsworth, Topological-sector fluctuations and ergodicity breaking at the Berezinskii-Kosterlitz-Thouless transition, *Phys. Rev. B* **91**, 155412 (2015).
- [63] S. V. Isakov, K. S. Raman, R. Moessner, and S. L. Sondhi, magnetization curve of spin ice in a [111] magnetic field, *Phys. Rev. B* **70**, 104418 (2004).
- [64] L. D. C. Jaubert, T. Lin, T. S. Opel, P. C. W. Holdsworth, and M. J. P. Gingras, Spin Ice Thin Film: Surface Ordering, Emergent Square Ice, and Strain Effects, *Phys. Rev. Lett.* **118**, 207206 (2017).
- [65] H. M. Revell, L. R. Yaraskavitch, J. D. Mason, K. A. Ross, H. M. L. Noad, H. A. Dabkowska, B. D. Gaulin, P. Henelius, and J. B. Kycia, Evidence of impurity and boundary effects

- on magnetic monopole dynamics in spin ice, *Nat. Phys.* **9**, 34 (2013).
- [66] L. Pili, S. A. Grigera, R. A. Borzi, A. Steppke, C. Hicks, and A. P. Mackenzie (unpublished).
- [67] J. Hamp, A. Chandran, R. Moessner, and C. Castelnovo, Emergent Coulombic criticality and Kibble-Zurek scaling in a topological magnet, *Phys. Rev. B* **92**, 075142 (2015).
- [68] S. Gao, O. Zaharko, V. Tsurkan, L. Prodan, E. Riordan, J. Lago, B. Fak, A. R. Wildes, M. M. Koza, C. Ritter, P. Fouquet, L. Keller, E. Canévet, M. Medarde, J. Blomgren, C. Johansson, S. R. Giblin, S. Vrtnik, J. Luzar, A. Loidl *et al.*, Dipolar Spin Ice States with a Fast Monopole Hopping Rate in CdEr_2X_4 ($X = \text{Se}, \text{S}$), *Phys. Rev. Lett.* **120**, 137201 (2018).
- [69] M. Hermele, M. P. A. Fisher, and L. Balents, Pyrochlore photons: The $U(1)$ spin liquid in a $S = 1/2$ three-dimensional frustrated magnet, *Phys. Rev. B* **69**, 064404 (2004).
- [70] R. Sibille, E. Lhotel, M. C. Hatnean, G. Balakrishnan, B. Fåk, N. Gauthier, T. Fennell, and M. Kenzelmann, Candidate quantum spin ice in the pyrochlore $\text{Pr}_2\text{Hf}_2\text{O}_7$, *Phys. Rev. B* **94**, 024436 (2016).
- [71] R. Sibille, N. Gauthier, H. Yan, M. C. Hatnean, J. Ollivier, B. Winn, U. Filges, G. Balakrishnan, M. Kenzelmann, N. Shannon, and T. Fennell, Experimental signatures of emergent quantum electrodynamics in $\text{Pr}_2\text{Hf}_2\text{O}_7$, *Nat. Phys.* **14**, 711 (2018).
- [72] J. A. M. Paddison, H. S. Ong, J. O. Hamp, P. Mukherjee, X. Bai, M. G. Tucker, N. P. Butch, C. Castelnovo, M. Mourigal, and S. E. Dutton, Emergent order in the kagome Ising magnet $\text{Dy}_3\text{Mg}_2\text{Sb}_3\text{O}_{14}$, *Nat. Commun.* **7**, 13842 (2016).
- [73] J. Carrasquilla, Z. Hao, and R. G. Melko, A two-dimensional spin liquid in quantum kagome ice, *Nat. Commun.* **6**, 7421 (2015).
- [74] T. A. Bojesen and S. Onoda, Quantum Spin Ice under a [111] Magnetic Field: From Pyrochlore to Kagome, *Phys. Rev. Lett.* **119**, 227204 (2017).
- [75] O. Benton, O. Sikora, and N. Shannon, Seeing the light: Experimental signatures of emergent electromagnetism in a quantum spin ice, *Phys. Rev. B* **86**, 075154 (2012).
- [76] M. J. P. Gingras and P. A. McClarty, Quantum spin ice: A search for gapless quantum spin liquids in pyrochlore magnets, *Rep. Prog. Phys.* **77**, 056501 (2014).
- [77] S. T. Bramwell, M. J. Harris, B. C. den Hertog, M. J. P. Gingras, J. S. Gardner, D. F. McMorrow, A. R. Wildes, A. L. Cornelius, J. D. M. Champion, R. G. Melko, and T. Fennell, Spin Correlations in $\text{Ho}_2\text{Ti}_2\text{O}_7$: A Dipolar Spin Ice System, *Phys. Rev. Lett.* **87**, 047205 (2001).
- [78] T. Fennell, O. A. Petrenko, B. Fak, S. T. Bramwell, M. Enjalran, T. Yavors'kii, M. J. P. Gingras, R. G. Melko, and G. Balakrishnan, Neutron scattering investigation of the spin ice state in $\text{Dy}_2\text{Ti}_2\text{O}_7$, *Phys. Rev. B* **70**, 134408 (2004).
- [79] P. Henelius, T. Lin, M. Enjalran, Z. Hao, J. G. Rau, J. Altosaar, F. Flicker, T. Yavors'kii, and M. J. P. Gingras, Refrustration and competing orders in the prototypical $\text{Dy}_2\text{Ti}_2\text{O}_7$ spin ice material, *Phys. Rev. B* **93**, 024402 (2016).
- [80] S. R. Giblin, M. Twengström, L. Bovo, M. Ruminy, M. Bartkowiak, P. Manuel, J. C. Andresen, D. Prabhakaran, G. Balakrishnan, E. Pomjakushina, C. Paulsen, E. Lhotel, L. Keller, M. Frontzek, S. C. Capelli, O. Zaharko, P. A. McClarty, S. T. Bramwell, P. Henelius, and T. Fennell, Pauling Entropy, Metastability, and Equilibrium in $\text{Dy}_2\text{Ti}_2\text{O}_7$ Spin Ice, *Phys. Rev. Lett.* **121**, 067202 (2018).
- [81] M. Twengström, P. Henelius, and S. T. Bramwell, Screening and the pinch point paradox in spin ice, *Phys. Rev. Research* **2**, 013305 (2020).
- [82] A. A. Turrini, Thermodynamic behavior of rare earth pyrochlores, Ph.D. thesis, Université de Genève, 2020.
- [83] A. S. Wills, R. Ballou, and C. Lacroix, Model of localized highly frustrated ferromagnetism: The *kagomé* spin ice, *Phys. Rev. B* **66**, 144407 (2002).
- [84] S. Zhang, I. Gilbert, C. Nisoli, G.-W. Chern, M. J. Erickson, L. O'Brien, C. Leighton, P. E. Lammert, V. H. Crespi, and P. Schiffer, Crystallites of magnetic charges in artificial spin ice, *Nature (London)* **500**, 553 (2013).
- [85] E. Mengotti, L. J. Heyderman, A. F. Rodríguez, F. Nolting, R. V. Hügli, and H.-B. Braun, Real-space observation of emergent magnetic monopoles and associated Dirac strings in artificial kagome spin ice, *Nat. Phys.* **7**, 68 (2011).
- [86] G. Möller and R. Moessner, Artificial Square Ice and Related Dipolar Nanoarrays, *Phys. Rev. Lett.* **96**, 237202 (2006).
- [87] O. Sendetskyi, V. Scagnoli, N. Leo, L. Anghinolfi, A. Alberca, J. Luning, U. Staub, P. M. Derlet, and L. J. Heyderman, Continuous magnetic phase transition in artificial square ice, *Phys. Rev. B* **99**, 214430 (2019).
- [88] B. C. den Hertog and M. J. P. Gingras, Dipolar Interactions and Origin of Spin Ice in Ising Pyrochlore Magnets, *Phys. Rev. Lett.* **84**, 3430 (2000).
- [89] S. K. Das, J. Horbach, K. Binder, M. E. Fisher, and J. V. Sengers, Static and dynamic critical behavior of a symmetrical binary fluid: A computer simulation, *J. Chem. Phys.* **125**, 024506 (2006).
- [90] F. Y. Wu, Remarks on the modified potassium dihydrogen phosphate model of a ferroelectric, *Phys. Rev.* **168**, 539 (1968).
- [91] G. I. Watson, Symmetry relations for the six-vertex model, *J. Stat. Phys.* **94**, 1045 (1999).
- [92] J. C. Bezdek, *Pattern Recognition with Fuzzy Objective Function Algorithms* (Springer US, New York, 1981).